

A framework for performance characterization of energy-resolving photon-counting detectors

Mats Persson^{a)}

Departments of Bioengineering and Radiology, Stanford University, Stanford 94305, California, USA

(Corresponding author. E-mail: matspers@stanford.edu)

Paurakh L. Rajbhandary

Departments of Electrical Engineering and Radiology, Stanford University, Stanford 94305, California, USA

Norbert J. Pelc

Departments of Electrical Engineering, Bioengineering and Radiology, Stanford University, Stanford 94305, California, USA

(Dated: 21 March 2018)

Purpose: Photon-counting energy resolving detectors are subject to intense research interest, and there is a need for a general framework for performance assessment of these detectors. The commonly used linear-systems theory framework, which measures detector performance in terms of noise-equivalent quanta (NEQ) and detective quantum efficiency (DQE) is widely used for characterizing conventional X-ray detectors but does not take energy-resolving capabilities into account. The purpose of this work is to extend this framework to encompass energy-resolving photon-counting detectors and elucidate how the imperfect energy response of real-world detectors affects imaging performance.

Method: We generalize NEQ and DQE to matrix-valued quantities as functions of spatial frequency, and show how these matrices can be calculated from simple Monte Carlo simulations. To demonstrate how the new metrics can be interpreted, we compute them for simplified models of fluorescence and Compton scatter in a photon-counting detector and for a Monte Carlo model of a CdTe detector with $0.5 \times 0.5 \text{ mm}^2$ pixels.

Results: Our results show that the ideal-linear-observer performance for any detection or material quantification task can be calculated from the proposed generalized NEQ and DQE metrics. Off-diagonal elements in these matrices are shown to be related to loss of energy information due to imperfect energy resolution. The Monte Carlo model of the CdTe detector predicts a zero-frequency dose efficiency relative to an ideal detector of 0.86 and 0.65 for detecting water and bone, respectively. When the task instead is to quantify these materials, the corresponding values are 0.34 for water and 0.26 for bone.

Conclusions: We have developed a framework for assessing the performance of photon-counting energy-resolving detectors and shown that the matrix-valued NEQ and DQE metrics contain sufficient information for calculating the dose efficiency for both detection or quantification tasks, the task having any spatial and energy dependence. This framework will be beneficial for the development of photon-counting X-ray detectors.

Key words: X-ray imaging, photon counting, spectral imaging, linear-systems theory, detective quantum efficiency, noise-equivalent quanta

I. INTRODUCTION

The development of energy-resolving photon-counting detectors for medical X-ray imaging is an active research field.¹⁻⁵ Systems with such detectors are currently commercially available for mammography⁶, and prototypes have been demonstrated for computed tomography (CT)⁷⁻¹⁰. An energy-resolving photon-counting detector uses several electronic threshold levels to separate the registered counts into energy bins depending on the deposited energy in each event. This enables spectroscopic imaging, i.e. using the information contained in the energy distribution of the incoming spectrum to obtain more information about the imaged object. The energy information can be used for improving the signal-difference-to-noise ratio (SDNR) by optimal weighting^{11,12}, for removing beam-hardening artifacts and for generating material-selective images.^{7,13,14}

The ongoing development of improved energy-resolving photon-counting X-ray detectors raises the question of how detector performance should be measured. Using a relevant metric is important in order to optimize and compare detector designs with different detector materials and pixel sizes or with different properties of the readout electronics such as the energy resolution and anti-coincidence logic.

The performance of conventional, non-energy-resolving X-ray detectors, such as energy-integrating detectors and photon-counting detectors without energy-resolving capabilities, is commonly measured in terms of the detective quantum efficiency (DQE).¹⁵ This metric, which is usually expressed as a function of spatial frequency, measures how well the detector is able to use the incoming photon statistics for each spatial frequency compared to an ideal detector. A closely related metric is the noise-equivalent quanta (NEQ), which measures the number of photons that an ideal detector would require in order to obtain the same signal-difference-to-noise ratio as the studied detector. An overview of the theory of DQE and NEQ for ordinary (non-spectral) detectors can be found in Ref. 16.

Several studies have been published previously on how to model the frequency-dependent detective quantum efficiency of photon-counting detectors,¹⁷⁻²⁰ but these studies do not take energy information into account. The impact of detector nonidealities on spectral imaging tasks has been studied by several authors²¹⁻²⁷. However, these publications only study the zero-spatial-frequency performance and do not investigate the frequency-dependent spectral performance. Shikhaliev et al.²⁸ studied the effect of characteristic X-rays on the spectrum

shape and on the spatial resolution. Richard and Siewerdsen²⁹ used linear-systems theory to study the performance of a dual-energy system. Also, the detectability for specific tasks with both spectral and spatial dependence has been studied by Fredenberg et al.³⁰, Yveborg et al.³¹ and Chen et al.³²

A common way to combine information from several spectral channels is to make a weighted sum of the energy-selective images, with weights chosen to be optimal for the considered imaging task.^{11,12,33} A good measure of the performance of an energy-resolving detector should therefore take optimal weighting into account. Taking the spatial-frequency dependence of the signal and noise into account when calculating optimal weights can improve detectability in an energy-weighted image, either by calculating an optimized weight for each image³⁴ or by letting the weights themselves be functions of spatial frequency³⁵. This is equivalent to applying different spatial filters to the different energy bin images before forming the weighted sum, an approach studied in the dual-energy case by Richard and Siewerdsen.²⁹

Another way to utilize spectral X-ray measurement is to perform basis material decomposition, which builds on the observation that the linear attenuation coefficient of any substance in the human body can be approximated well as a linear combination of a small number of basis functions, typically two, or three in the presence of a high-atomic-number contrast agent with a K-edge in the diagnostic energy range. Basis material decomposition then amounts to using the energy-resolved X-ray data to estimate the amount of each of these basis materials along each projection line, thereby completely characterizing the energy-dependent attenuation of the object.^{13,14} This is useful in particular for CT, to remove beam-hardening artifacts and characterize object composition.

The purpose of this work is to present a general framework for comparing the performance of energy-resolving imaging detectors, encompassing both energy-weighting and material-decomposition performance. To this end, we derive an expression for the detectability achieved by an ideal linear observer, taking into account the full spatial-frequency dependence of the available energy information. We also propose generalized NEQ and DQE metrics for measuring energy-resolving detector performance. To show how the proposed metrics can be used in practice, we apply the developed framework to simple models of detectors with nonideal energy response and to a more realistic simulation model of a photon-counting detector.

II. THEORY

II.A. Matrix-valued NEQ and DQE

TABLE I: List of symbols and their dimensions. L: length; E: energy.

Symbol	Dimension	Description
*		Complex conjugate
†		Conjugate-transpose
A	L	Basis coefficient line integral
\tilde{A}	L^3	Fourier transform of A
d	1	Presampling detected signal
D	L^2	Fourier transform of d
d^s	1	Sampled signal as discrete sequence
D^s	1	Discrete-space Fourier transform of d^s
d^+	L^{-2}	Sampled signal as delta-pulse train
d'	1	Optimal-linear-observer detectability
DQE	E^{-1}	Detective quantum efficiency matrix in energy basis
DQE^B	1	Detective quantum efficiency matrix in material basis
Δ_x, Δ_y	L	Detector pixel width and height
E	E	Incident energy of photon
ε	E	Registered energy in event
$F_{\tilde{A}}$	L^6	Fisher information matrix for \tilde{A}
\mathcal{F}		Continuous Fourier transformation
\mathcal{F}_{DS}		Discrete-space Fourier transformation
f	L^{-1}	Material basis function
\overline{G}	1	Large-area gain
h	L^{-2}	Point-spread function
H	1	Transfer function
H^B	1	Rescaled transfer matrix in material basis
K_d	1	Cross-covariance matrix of d

K_{d^+}	L^{-4}	Cross-covariance matrix of d^+
K^s	1	Cross-covariance matrix of d^s
L	1	Basis transformation matrix element
MTF_{pre}	1	Presampling modulation transfer function
$\mathbf{n} = (n_x, n_y)$	1	Discrete pixel coordinate
NEQ	$L^{-2}\text{E}^{-2}$	Noise-equivalent quanta matrix in energy basis
NEQ^{B}	L^{-2}	Noise-equivalent quanta matrix in material basis
Nyq		Nyquist region of the (u,v) plane
Φ	$L^{-2}\text{E}^{-1}$	Prepatient photons per area and energy
q	$L^{-2}\text{E}^{-1}$	Incident photons per area and energy
\bar{q}^{tot}	L^{-2}	Total incident photons per area
Q	E^{-1}	Fourier transform of q
$\mathbf{r} = (x, y)$	L	Position on detector
$\mathbf{r}_{\mathbf{n}}$	L	Pixel center position
$\Delta\mathbf{S}$	L^2	Task function in energy basis
$\Delta\mathbf{S}^{\text{B}}$	L^2	Task function in material basis
\mathbf{T}	1	Matrix mapping \mathbf{X} to $(\mathbf{X}, \mathbf{X}^*)^{\text{T}}$
$\mathbf{u} = (u, v)$	L^{-1}	Spatial frequency
W^s	1	Cross-spectral density of d^s
W_{d^+}	L^{-2}	Cross-spectral density of d^+
\bar{X}		Expected value of X

In the following, we will use parentheses to denote that a quantity is a function of a continuous variable and use subscripts when the variable is discrete. Most of our notation is similar to Ref. 16 and 18. Consider a situation where a distribution of X-ray photons is incident on a detector. Let $q(\mathbf{r}, E)$ be a random process describing the number of incident photons per area and energy as a function of position $\mathbf{r} = (x, y)^{\text{T}}$ and energy E . This photon distribution is measured by an energy-resolving detector and registered as counts in energy bins $d_{\mathbf{n},k}^s$ where $\mathbf{n} = (n_x, n_y)^{\text{T}}$ is the discrete coordinate of a detector pixel in the (x, y) plane and $k = 1, \dots, N_b$ is the index of the energy bin. To avoid boundary effects, we assume that

the detector and the photon distribution are of infinite extent. Both q and d^s are random processes, and their expected values will be denoted by \bar{q} and \bar{d}^s , respectively. It is also useful to define a presampling detected signal $d_k(\mathbf{r})$, whose value at every point \mathbf{r} is the number of counts that would be registered in each energy bin k by a fictitious pixel centered at \mathbf{r} . Therefore, $d_{\mathbf{n},k}^s = d_k(\mathbf{r}_{\mathbf{n}})$ where $\mathbf{r}_{\mathbf{n}} = (n_x\Delta_x, n_y\Delta_y)^\top$ is the center of pixel \mathbf{n} and Δ_x and Δ_y are the pixel center-to-center distances in the x and y directions, respectively.

The continuous Fourier transform of $q(\mathbf{r}, E)$ with respect to \mathbf{r} is a random process given by $Q(\mathbf{u}, E) = \mathcal{F}[q(\mathbf{r}, E)](\mathbf{u}, E) = \int_{\mathbb{R}^2} q(\mathbf{r}, E)e^{-2\pi i\mathbf{u}\cdot\mathbf{r}}d\mathbf{r}$, and $D_k(\mathbf{u})$ is defined analogously as the transform of $d_k(\mathbf{r})$. The 2D discrete-space Fourier transform of $d_{\mathbf{n},k}^s$ with respect to \mathbf{n} is given by $D_k^s(\mathbf{u}) = \mathcal{F}_{\text{DS}}[d_{\mathbf{n},k}^s](\mathbf{u}) = \sum_{\mathbf{n}=-\infty}^{\infty} d_{\mathbf{n},k}^s e^{-2\pi i\mathbf{u}\cdot\mathbf{r}_{\mathbf{n}}}$. We now assume that the system is linear and shift-invariant, which allows us to introduce the system point-spread function for the k^{th} energy bin $h_k(\Delta\mathbf{r}, E)$ that relates the expected values of the the incoming photon distribution and the registered count distribution:

$$\bar{d}_k(\mathbf{r}) = \Delta_x\Delta_y \int_{\mathbb{R}^2} \int_0^{E_{\max}} h_k(\mathbf{r} - \mathbf{r}', E)\bar{q}(\mathbf{r}', E)dE d\mathbf{r}', \quad (1)$$

where E_{\max} is the maximum incident energy. Here, the pixel cell area $\Delta_x\Delta_y$ has been broken out of the definition of $h_k(\Delta\mathbf{r}, E)$, meaning that h_k can be interpreted as a presampling distribution of registered quanta per unit pixel area in the k^{th} energy bin when the input signal $\bar{q}(\mathbf{r}, E)$ is a beam incident on a single point of the detector. $h_k(\Delta\mathbf{r}, E)$ thus contains information about both the quantum detection efficiency and the spatial resolution of the detector. Denoting the Fourier transform of h_k with respect to Δx and Δy by H_k ,

$$\bar{D}_k(\mathbf{u}) = \Delta_x\Delta_y \int_0^{E_{\max}} H_k(\mathbf{u}, E)\bar{Q}(\mathbf{u}, E)dE. \quad (2)$$

In analogy with conventional X-ray detectors, it is possible to define a presampling modulation transfer function $[\text{MTF}_{\text{pre}}]_k(\mathbf{u}, E) = |H_k(\mathbf{u}, E)/H_k(\mathbf{0}, E)|$ for each incident energy and for each energy bin.

To calculate the performance of the detector for a given imaging task, we also need to know the covariance between different measurements $d_{\mathbf{n},k}^s$. Assuming that the noise is wide-sense stationary, this is given by the cross-covariance matrix K^s with elements

$$K_{\Delta\mathbf{n},k,k'}^s = \text{Cov}(d_{\mathbf{n},k}^s, d_{\mathbf{n}+\Delta\mathbf{n},k'}^s). \quad (3)$$

The cross-spectral density of $d_{\mathbf{n},k}^s$ can then be calculated as

$$W_{k,k'}^s(\mathbf{u}) = \sum_{\Delta\mathbf{n}=-\infty}^{\infty} K_{\Delta\mathbf{n},k,k'}^s e^{-2\pi i(\mathbf{u}\cdot\Delta\mathbf{r}_{\mathbf{n}})}, \quad (4)$$

where $\Delta\mathbf{r}_{\mathbf{n}} = \mathbf{r}_{\mathbf{n}+\Delta\mathbf{n}} - \mathbf{r}_{\mathbf{n}}$. For $k = k'$, $W_{k,k'}^s(\mathbf{u})$ is the noise power spectrum (NPS) in energy bin k , whereas $W_{k,k'}^s(\mathbf{u})$ for $k \neq k'$ describes the frequency dependence of correlations between different energy bins.

Now assume that the studied detector is used to discriminate between two cases: a object-absent (background) case with incident photon distribution $q(\mathbf{r}, E)$ and an object-present case where the incident photon distribution is $q^{\text{obj}}(\mathbf{r}, E) = q(\mathbf{r}, E) + \Delta q(\mathbf{r}, E)$, i.e. a signal-known-exactly/background-known-exactly (SKE/BKE) task. The difference in the expected presampled signal between the two cases is $\Delta\bar{d}_{\mathbf{n},k}$ with the Fourier transform

$$\Delta\bar{D}_k(\mathbf{u}) = \Delta_x \Delta_y \int_0^{E_{\text{max}}} H_k(\mathbf{u}, E) \Delta\bar{Q}(\mathbf{u}, E) dE, \quad (5)$$

where $\Delta\bar{Q}(\mathbf{u}, E)$ is the expected signal difference in the Fourier domain. The expected difference in the sampled signal is $\Delta\bar{d}_{\mathbf{n},k}^s$ with the discrete-space Fourier transform $\Delta\bar{D}_k^s(\mathbf{u}) = \frac{1}{\Delta_x \Delta_y} \sum_{m_u, m_v=-\infty}^{\infty} \Delta\bar{D}_k(u - \frac{m_u}{\Delta_x}, v - \frac{m_v}{\Delta_y})$.

Our measure of the detector performance for this task will be squared signal-difference-to-noise ratio (“detectability”) d'^2 of the optimal linear observer, which tells us how well this model observer can discriminate between the two cases (object present or absent) given the available measurements in all pixels and all energy bins. Viewing $\bar{d}_{\mathbf{n},k}^s$ and $\Delta\bar{d}_{\mathbf{n},k}^s$ for all k and \mathbf{n} as elements of vectors \mathbf{d}^s and $\Delta\bar{\mathbf{d}}^s$ (see Sec. 13.2.12 of Ref. 36), d'^2 can be expressed as

$$d'^2 = \left(\Delta\bar{\mathbf{d}}^s\right)^\top \text{Cov}(\mathbf{d}^s)^{-1} \Delta\bar{\mathbf{d}}^s. \quad (6)$$

By changing basis using the discrete-space Fourier transform \mathcal{F}_{DS} , this expression is transformed into (see appendix A)

$$d'^2 = \Delta_x \Delta_y \int_{\text{Nyq}} \sum_k \sum_{k'} \Delta\bar{D}_k^s(\mathbf{u})^* [(W^s)^{-1}]_{k,k'}^* (\mathbf{u}) \Delta\bar{D}_{k'}^s(\mathbf{u}) d\mathbf{u}, \quad (7)$$

where $*$ denotes complex conjugate and Nyq denotes the Nyquist region $\left\{ \mathbf{u} : |u| < \frac{1}{2\Delta_x}, |v| < \frac{1}{2\Delta_y} \right\}$.

The ideal-linear-observer performance is thus obtained as an integral over spatial frequencies of a quadratic form in $\Delta\bar{\mathbf{D}}^s = (\Delta\bar{D}_k^s(\mathbf{u}))$, the difference vector of registered counts

in all energy bins for all spatial frequencies \mathbf{u} . To attain this performance limit, the model observer needs to take data from all the energy bins into account, which is difficult for a human observer. For any given task, however, frequency-dependent optimal weighting of the energy bin images can be used to form a single image which attains the same performance for that task.³⁵

We will now express (7) in a way that separates parameters specific to the detector from parameters specific to the discrimination task. To do this, we need to assume that signal aliasing is negligible, so that $\Delta\bar{D}_k^s(\mathbf{u}) \approx \frac{1}{\Delta_x\Delta_y}\Delta\bar{D}_k(\mathbf{u})$. This is true if the pixel size is sufficiently small compared to other resolution-limiting factors, such as the detector point-spread function or the focal spot size, or if an oversampling scheme is used i.e. several measurements are performed for different detector positions relative to the object. To obtain an expression that is easily comparable to non-pixelated systems, we will express the noise correlations in terms of W_{d^+} , the cross-spectral density of the sampled pulse train signal $d_k^+(\mathbf{r}) = \sum_{\mathbf{n}=-\infty}^{\infty} d_{\mathbf{n},k}^s\delta(\mathbf{r} - \mathbf{r}_{\mathbf{n}})$. By observing that $K_{\Delta\mathbf{n},k,k'}^s = (K_d)_{k,k'}(\Delta\mathbf{r}_{\mathbf{n}})$, where K_d is the autocovariance of the presampling signal d , and using $(K_{d^+})_{k,k'}(\Delta\mathbf{r}) = \frac{1}{\Delta_x\Delta_y}(K_d)_{k,k'}(\Delta\mathbf{r})\sum_{\mathbf{n}}\delta(\Delta\mathbf{r} - \Delta\mathbf{r}_{\mathbf{n}})$ (Ref. 16, eq. 2.108), we obtain $W_{k,k'}^s(\mathbf{u}) = \Delta_x\Delta_y(W_{d^+})_{k,k'}(\mathbf{u})$. This allows (7) to be expressed as

$$d'^2 = \int_{\text{Nyq}} \sum_k \sum_{k'} \int_0^{E_{\max}} \int_0^{E_{\max}} H_k(\mathbf{u}, E)^* \Delta\bar{Q}(\mathbf{u}, E)^* \cdot [W_{d^+}^{-1}]_{k,k'}^*(\mathbf{u}) H_k(\mathbf{u}, E') \Delta\bar{Q}(\mathbf{u}, E') dE dE' d\mathbf{u}. \quad (8)$$

To rewrite (8) in a form that is more similar to the corresponding expression for a conventional detector, we introduce the relative signal difference $\Delta S(\mathbf{u}, E) = \Delta\bar{Q}(\mathbf{u}, E)/\bar{q}(E)$ and define a frequency-dependent matrix $\text{NEQ}(\mathbf{u})$ with elements given by

$$\text{NEQ}(\mathbf{u}, E, E') = \sum_k \sum_{k'} \bar{q}(E) H_k(\mathbf{u}, E)^* [W_{d^+}^{-1}]_{k,k'}^*(\mathbf{u}) H_{k'}(\mathbf{u}, E') \bar{q}(E'). \quad (9)$$

This gives

$$d'^2 = \int_{\text{Nyq}} \int_0^{E_{\max}} \int_0^{E_{\max}} \Delta S(\mathbf{u}, E)^* \text{NEQ}(\mathbf{u}, E, E') \Delta S(\mathbf{u}, E') dE dE' d\mathbf{u}, \quad (10)$$

which is analogous to the formula for conventional X-ray detectors (Ref. 16, Eq. 2.150, for non-pixelated detectors):

$$d'^2 = \int |\Delta S(\mathbf{u})|^2 \text{NEQ}(\mathbf{u}) d\mathbf{u}, \quad (11)$$

where (Ref. 16, Eqs. 2.193 and 2.209)

$$\text{NEQ} = \frac{\bar{q}^2 \bar{G}^2 \text{MTF}_{\text{pre}}^2(\mathbf{u})}{\text{NPS}_{\text{dig}}(\mathbf{u})} = \frac{\bar{q}^2 \bar{G}^2 \text{MTF}_{\text{pre}}^2(\mathbf{u})}{\Delta_x^2 \Delta_y^2 \text{NPS}_{d^+}(\mathbf{u})} = \frac{\bar{q}^2 H^2(\mathbf{u})}{\text{NPS}_{d^+}(\mathbf{u})}. \quad (12)$$

In this equation, \bar{G} is the large-area gain (average registered counts per pixel divided by \bar{q}), MTF_{pre} is the presampling modulation transfer function and $|H(\mathbf{u})| = \bar{G} \text{MTF}_{\text{pre}} / (\Delta_x \Delta_y)$ is a transfer function defined in analogy with $H_k(\mathbf{u}, E)$.

$\text{NEQ}(\mathbf{u})$ is thus a natural generalization of the noise-equivalent quanta used to describe conventional detectors. It is a frequency-dependent matrix with continuous indices E and E' encoding all the information about the detector that is relevant for evaluating the detection performance. It depends on the background case noise characteristics, and thus on the incident spectrum in that setting, but not on the discrimination task. The discrimination task function ΔS determines how the different frequency components of NEQ are weighted together to give the detectability. The NEQ matrix therefore defines a quadratic form in $\Delta S(\mathbf{u})$ giving the contribution to d'^2 at each spatial frequency.

The above description applies to a continuous-to-discrete imaging system, which is the relevant type of system for multibin photon-counting detectors. Note, however, that the analysis, apart from the sampling step, can be adapted to a continuous-to-continuous imaging system by replacing n_x , n_y and k by continuous variables. An *ideal* energy-resolving imaging system is a continuous-to-continuous imaging system that registers the correct position and energy for each incoming photon. Its transfer function is therefore $H(\mathbf{u}, E, \varepsilon) = \delta(E - \varepsilon)$, where ε denotes the registered energy, and its noise cross-spectrum is white, i.e. $W_q(\mathbf{u}, \varepsilon, \varepsilon')$ is constant with respect to \mathbf{u} . For an ideal photon-counting detector, the input signal is Poisson distributed and the registered counts at different energies are uncorrelated, so that $W_q(\mathbf{u}, \varepsilon, \varepsilon') = \bar{q}(\varepsilon) \delta(\varepsilon - \varepsilon')$ where $\bar{q}(\varepsilon)$ is the expected number of incident photons per energy and area (Ref. 16, Sec. 2.6.2.3). For a pixelated but otherwise ideal detector, $W_{d^+}(\mathbf{u}, \varepsilon, \varepsilon')$ tends to $W_q(\mathbf{u}, \varepsilon, \varepsilon')$ as Δ_x and Δ_y tend to 0, which gives $\text{NEQ}^{\text{ideal}}(\mathbf{u}, E, E') = \bar{q}(E) \delta(E - E')$ for an ideal detector.

In analogy with the conventional definition of DQE, $\text{DQE}(\mathbf{u}) = \text{NEQ}(\mathbf{u})/\bar{q}$, we can now define a DQE matrix by normalizing **NEQ** by the ideal-detector performance. Therefore, let

$$\text{DQE}(\mathbf{u}, E, E') = \bar{q}(E)^{-1/2} \text{NEQ}(\mathbf{u}, E, E') \bar{q}(E')^{-1/2}, \quad (13)$$

or equivalently,

$$\text{DQE}(\mathbf{u}, E, E') = \bar{q}(E)^{1/2} \left[\sum_k \sum_{k'} H_k(\mathbf{u}, E)^* [W_{d^+}^{-1}]_{k,k'}^*(\mathbf{u}) H_{k'}(\mathbf{u}, E') \right] \bar{q}(E')^{1/2} \quad (14)$$

This definition gives $\text{DQE}^{\text{ideal}}(\mathbf{u}, E, E') = \delta(E - E')$ for the ideal detector. The fact that no detector performs better than an ideal one is now formulated as $\text{NEQ} \leq \text{NEQ}^{\text{ideal}}$ where \leq should be interpreted in the matrix inequality sense, i.e. $\mathbf{A} \leq \mathbf{B}$ if $\mathbf{B} - \mathbf{A}$ is positive semidefinite. Proving this inequality mathematically would require analyzing how the noise cross-spectral density is related to the signal transfer function, e.g. using cascaded systems analysis,¹⁶ which is beyond the scope of this work. We therefore view it as a physically motivated requirement that any realistic detector model must satisfy.

As a simple example of a nonideal detector, consider a detector that has imperfect quantum detection efficiency $\eta(E) < 1$ but infinitely high spatial resolution and perfect energy response. For this detector, $\text{NEQ}(\mathbf{u}, E, E') = \eta(E)\bar{q}(E)\delta(E - E')$ and $\text{DQE}(\mathbf{u}, E, E') = \eta(E)\delta(E - E')$. Our definition of DQE can thus be seen as a generalization of the energy-dependent detection efficiency $\eta(E)$.

The diagonal elements of the DQE matrix can be interpreted as the dose efficiency per energy for detecting a spectrum change at one single energy, whereas the off-diagonal terms reflect the degree to which different detected energies interfere with each other. This interference may be constructive or destructive, depending on whether the off-diagonal terms are positive or negative. To understand why the DQE matrix has dimensions of inverse energy unlike the conventional DQE which is dimensionless, note that a task function which equals $\Delta S(\mathbf{u}) = \Delta S_0$ in a small interval ΔE around a single energy E_0 gives $d'^2(\mathbf{u}) \approx \bar{q}(E_0)\text{DQE}(\mathbf{u}, E_0, E_0)\Delta E^2 \Delta S_0^2$, which can be compared to $d_{\text{ideal}}'^2(\mathbf{u}) \approx \bar{q}(E_0)\Delta E \Delta S_0^2$ for the ideal detector. $\text{DQE}^{\text{task}} = d'^2(\mathbf{u})/d_{\text{ideal}}'^2(\mathbf{u}) \approx \text{DQE}(\mathbf{u}, E_0, E_0)\Delta E$ is thus proportional to ΔE if $\text{DQE}(\mathbf{u}, E_0, E_0)$ is nonsingular. This is the case for binning detectors since these have difficulty detecting a change in a narrow energy band measured in a background of noise contributions from a wide energy interval.

II.B. NEQ and DQE in material basis

The NEQ matrix contains information about the performance of the detector for any spectral discrimination task. In practice, this matrix would be cumbersome to report in e.g. a publication, especially if the energy scale is discretized into a large number of steps. For example, if the energy variable is discretized in 1 keV-steps from 0 to 140 keV, one needs to supply a 140×140 matrix as a function of spatial frequency in order to characterize the detector performance. However, the NEQ matrix can be expressed more compactly by exploiting the basis material concept i.e. the approximation that all substances likely to be present in the field of view have attenuation coefficients $\mu(E)$ in a low-dimensional space, spanned by a small number N_m of basis functions $f_l(E)$: $\mu(E) = \sum_{l=1}^{N_m} a_l f_l(E)$.¹³ As long as one is only interested in the detector performance for differentiating materials whose attenuation coefficients lie within this space, and as long as the signal difference is small enough that a linearized description may be used, one only needs to know the restriction of the NEQ matrix to this subspace to be able to predict the performance for the relevant tasks.

For a homogeneously illuminated object and in the absence of detected scatter from the object, we can assume that the photon distribution incident on the detector is given by

$$\bar{q}(\mathbf{r}, E) = \Phi(E) \exp \left(- \sum_{l=1}^{N_m} A_l(\mathbf{r}) f_l(E) \right), \quad (15)$$

where $\Phi(E)$ is the number of photons per area and energy incident on the object and $A_l(\mathbf{r})$ are the basis coefficients integrated along the X-ray beam path. We will study the task of differentiating between two situations, $A_l^{\text{bg}}(\mathbf{r})$ and $A_l^{\text{obj}}(\mathbf{r}) = A_l^{\text{bg}}(\mathbf{r}) + \Delta A(\mathbf{r})$, both small perturbations of a homogeneous baseline $A_l(\mathbf{r}) = A_l^0$. In the small-signal approximation, $\bar{q}^{\text{obj}}(\mathbf{r}, E) \approx \bar{q}(E) + \sum_{l=1}^{N_m} \frac{\partial \bar{q}(E)}{\partial A_l} (A_l^{\text{obj}}(\mathbf{r}) - A_l^0)$, and similarly for $\bar{q}^{\text{bg}}(\mathbf{r}, E)$. Here, $\bar{q}(E)$ is the expected photon flux at the detector, given by (15) for $A_l(\mathbf{r}) = A_l^0$, $l = 1, \dots, N_m$ and the derivative $\frac{\partial \bar{q}(E)}{\partial A_l}$ is evaluated for $A_l = A_l^0$. The difference in expected photon flux between the two cases is approximately $\Delta \bar{q}(\mathbf{r}, E) = \sum_{l=1}^{N_m} \frac{\partial \bar{q}(E)}{\partial A_l} \Delta A_l(\mathbf{r})$. Letting $\tilde{A}(\mathbf{u})$ denote the continuous Fourier transform of A ,

$$\Delta \bar{Q}(\mathbf{u}, E) = \sum_{l=1}^{N_m} \frac{\partial \bar{q}(E)}{\partial A_l} \Delta \tilde{A}_l(\mathbf{u}) \quad (16)$$

and

$$\Delta S(\mathbf{u}, E) = \sum_{l=1}^{N_m} L_l^{\mathcal{B}}(E) \frac{1}{\bar{q}^{\text{tot}}} \frac{\partial \bar{q}^{\text{tot}}}{\partial A_l} \Delta \tilde{A}_l(\mathbf{u}) = \sum_{l=1}^{N_m} L_l^{\mathcal{B}}(E) \Delta S_l^{\mathcal{B}}(\mathbf{u}), \quad (17)$$

where we have defined $L_l^{\mathcal{B}}(E) = \frac{\bar{q}^{\text{tot}}}{\bar{q}(E)} \frac{\partial \bar{q}(E)}{\partial A_l} / \frac{\partial \bar{q}^{\text{tot}}}{\partial A_l}$ with $\bar{q}^{\text{tot}} = \int_0^{E_{\text{max}}} \bar{q}(E) dE$. $L_l^{\mathcal{B}}(E)$ can be regarded as an element of a transformation matrix from the basis of individual energies to the basis \mathcal{B} of differential spectrum changes corresponding to differential path length changes of basis materials $\{f_1, f_2, \dots, f_{N_m}\}$. We have also defined the signal difference vector in the basis \mathcal{B} , $\Delta \mathbf{S}^{\mathcal{B}}(\mathbf{u})$, by $\Delta S_l^{\mathcal{B}}(\mathbf{u}) = \frac{1}{\bar{q}^{\text{tot}}} \frac{\partial \bar{q}^{\text{tot}}}{\partial A_l} \Delta \tilde{A}_l(\mathbf{u})$. Eq. 10 can now be expressed as

$$\begin{aligned} d'^2 &= \frac{1}{\bar{q}^{\text{tot}^2}} \int_{\text{Nyq}} \sum_l \sum_{l'} \Delta \tilde{A}_l(\mathbf{u})^* \frac{\partial \bar{q}^{\text{tot}}}{\partial A_l} \text{NEQ}_{l,l'}^{\mathcal{B}}(\mathbf{u}) \frac{\partial \bar{q}^{\text{tot}}}{\partial A_{l'}} \Delta \tilde{A}_{l'}(\mathbf{u}) d\mathbf{u} \\ &= \int_{\text{Nyq}} \Delta \mathbf{S}^{\mathcal{B}}(\mathbf{u})^\dagger \text{NEQ}^{\mathcal{B}}(\mathbf{u}) \Delta \mathbf{S}^{\mathcal{B}}(\mathbf{u}) d\mathbf{u}, \end{aligned} \quad (18)$$

where the matrix elements of the NEQ matrix in basis \mathcal{B} are given by

$$\text{NEQ}_{l,l'}^{\mathcal{B}}(\mathbf{u}) = \int_0^{E_{\text{max}}} \int_0^{E_{\text{max}}} L_l^{\mathcal{B}}(E) \text{NEQ}(\mathbf{u}, E, E') L_{l'}^{\mathcal{B}}(E') dE dE', \quad (19)$$

or, in a form that is easier to compute:

$$\text{NEQ}_{l,l'}^{\mathcal{B}}(\mathbf{u}) = \sum_k \sum_{k'} H_{k,l}^{\mathcal{B}}(\mathbf{u})^* [W_{d^+}^{-1}]_{k,k'}^* H_{k',l'}^{\mathcal{B}}(\mathbf{u}). \quad (20)$$

Here, $H_{k,l}^{\mathcal{B}}(\mathbf{u}) = \int_{E=0}^{E_{\text{max}}} \bar{q}^{\text{tot}} \left(\frac{\partial \bar{q}(E)}{\partial A_l} / \frac{\partial \bar{q}^{\text{tot}}}{\partial A_l} \right) H_k(\mathbf{u}, E) dE$ is the transfer function, relating the magnitude of a small relative modulation of the input photon fluence corresponding to a change in A_l at spatial frequency \mathbf{u} to the resulting change in registered counts per area in energy bin k at that frequency.

Like the NEQ for non-energy resolving detectors, $\text{NEQ}^{\mathcal{B}}$ has units of area^{-1} . Each diagonal component $\text{NEQ}_{ll}^{\mathcal{B}}$ of the latter specifies the number of quanta per area that an ideal detector needs to measure to achieve the same detectability as the studied detector, when the task is to detect the addition of a small amount of basis material l . The DQE matrix in basis \mathcal{B} is defined in analogy with (13):

$$\text{DQE}_{l,l'}^{\mathcal{B}}(\mathbf{u}) = \frac{\text{NEQ}_{l,l'}^{\mathcal{B}}(\mathbf{u})}{\sqrt{\text{NEQ}_{l,l}^{\mathcal{B},\text{ideal}} \cdot \text{NEQ}_{l',l'}^{\mathcal{B},\text{ideal}}}}, \quad (21)$$

where our notation reflects that $\text{NEQ}^{\mathcal{B},\text{ideal}}$ is independent of spatial frequency. The DQE defined in this way is a dose-normalized quantity that encodes the performance of the detector for all different tasks. For any specific detection task, the performance relative to an ideal detector is given by the task-specific DQE, which is a scalar-valued quantity:

$$\begin{aligned} \text{DQE}^{\text{task}}(\mathbf{u}) &= \frac{d'^2(\mathbf{u})}{d_{\text{ideal}}'^2(\mathbf{u})} = \frac{\int_0^{E_{\text{max}}} \int_0^{E_{\text{max}}} \Delta S(\mathbf{u}, E)^* \text{NEQ}(\mathbf{u}, E, E') \Delta S(\mathbf{u}, E') dE dE'}{\int_0^{E_{\text{max}}} |\Delta S(\mathbf{u}, E)|^2 \bar{q}(E) dE} \quad (22) \\ &= \frac{\Delta \mathbf{S}^{\mathcal{B}}(\mathbf{u})^\dagger \text{NEQ}^{\mathcal{B}}(\mathbf{u}) \Delta \mathbf{S}^{\mathcal{B}}(\mathbf{u})}{\Delta \mathbf{S}^{\mathcal{B}}(\mathbf{u})^\dagger \text{NEQ}^{\mathcal{B},\text{ideal}}(\mathbf{u}) \Delta \mathbf{S}^{\mathcal{B}}(\mathbf{u})}, \end{aligned}$$

where we have used the notation $d'^2(\mathbf{u})$ for the d'^2 contribution from frequency \mathbf{u} . Eq. 22 shows that DQE^{task} for detecting a small difference at frequency \mathbf{u} in one of the basis materials used in the decomposition, basis material l , is simply given by the diagonal element $\text{DQE}_{l,l}^{\mathcal{B}}(\mathbf{u})$ of $\text{DQE}^{\mathcal{B}}$. DQE^{task} for detecting differences due to a material with another spectral response can be obtained by expressing the DQE matrix in any basis which includes the linear attenuation of that feature as a basis function. When transforming to another basis of differential spectrum changes, NEQ transforms according to the normal rules for coordinate changes of quadratic forms, but there is no simple transformation rule for DQE since its components are obtained as ratios of components of two matrices both of which are basis-dependent.

For a given basis \mathcal{B} , the diagonal elements of $\text{DQE}^{\mathcal{B}}$ tell us how efficient the detector is for detecting a change in only one of the basis functions, while the off-diagonal terms specify the degree of constructive or destructive interference when the task involves detecting a difference in two or more basis functions. A positive off-diagonal term corresponds to a positive interference effect on detectability when both basis material path lengths are increased simultaneously.

Eq. 22 can be used to calculate the maximum and minimum DQE^{task} for any detection task. The change of variables $\Delta \mathbf{S}^{\mathcal{B}'}(\mathbf{u}) = [\text{NEQ}^{\mathcal{B},\text{ideal}}(\mathbf{u})]^{1/2} \Delta \mathbf{S}^{\mathcal{B}}(\mathbf{u})$ transforms (22) into

$$\text{DQE}^{\text{task}}(\mathbf{u}) = \left[\Delta \mathbf{S}^{\mathcal{B}'}(\mathbf{u})^\dagger \text{NEQ}^{\mathcal{B},\text{ideal}}(\mathbf{u})^{\dagger-1/2} \text{NEQ}^{\mathcal{B}}(\mathbf{u}) \text{NEQ}^{\mathcal{B},\text{ideal}}(\mathbf{u})^{-1/2} \Delta \mathbf{S}^{\mathcal{B}'}(\mathbf{u}) \right] / \left\| \Delta \mathbf{S}^{\mathcal{B}'} \right\|^2, \quad (23)$$

with maximum and minimum values given by the eigenvalues of

$$\text{NEQ}^{\mathcal{B},\text{ideal}}(\mathbf{u})^{\dagger-1/2} \text{NEQ}^{\mathcal{B}}(\mathbf{u}) \text{NEQ}^{\mathcal{B},\text{ideal}}(\mathbf{u})^{-1/2}.$$

II.C. Material decomposition

We now leave the study of detection-task performance for a moment and turn to another question: how well can the material composition of an object be quantified using measurements with the detector? One could try to estimate $A_l(\mathbf{r})$ directly, but a more fruitful approach is to estimate its Fourier transform $\tilde{A}_l(\mathbf{u})$. A limit on estimation performance is given by the Cramér-Rao lower bound (CRLB), which gives a lower limit of the covariance matrix of the estimated parameter for any unbiased estimator and has been shown to be a useful tool for analyzing estimation accuracy for spectral CT tasks³⁷. Although the CRLB only provides a lower bound, in practice the variance of the maximum likelihood estimator usually agrees well with the CRLB for material decomposition tasks, as has been shown in simulations³⁸. The authors are not aware of a tractable form for the CRLB for correlated Poisson variables in general, but as long as there are at least a few tens of photons in every energy bin and measurement, one can approximate the joint probability distribution of the bin counts as multivariate Gaussian. This approximation is valid both with and without pileup taken into account, but in the pileup-free case both mean and variance of each individual measurement will be equal to $d_{\mathbf{n},k}^s$. The components of the Fisher information matrix \mathbf{F}_θ for a real-valued vector parameter θ from a measured multivariate Gaussian random variable with mean μ and covariance matrix Σ is given by:³⁹

$$[\mathbf{F}_\theta]_{ij} = \left(\frac{\partial \mu}{\partial \theta_i} \right)^\top \Sigma^{-1} \frac{\partial \mu}{\partial \theta_j} + \text{Tr} \left(\Sigma^{-1} \frac{\partial \Sigma}{\partial \theta_i} \Sigma^{-1} \frac{\partial \Sigma}{\partial \theta_j} \right). \quad (24)$$

The CRLB now states that $\text{Cov}(\hat{\theta}) \geq \mathbf{F}_\theta^{-1}$ for any unbiased estimator $\hat{\theta}$ of θ .

In our case, μ and Σ are the mean and covariance of the measured counts vector \mathbf{d}^s , while the parameter $\theta = \left(\text{Re } \tilde{\mathbf{A}}, \text{Im } \tilde{\mathbf{A}} \right)^\top$ to be estimated contains the real and imaginary parts of the vector $\tilde{\mathbf{A}}$ obtained by concatenating the vectors $\tilde{\mathbf{A}}(\mathbf{u})$ for all spatial frequencies in the intersection of the right half-plane $\{\mathbf{u} : u > 0 \text{ or } u = 0, v > 0\}$ and the Nyquist region. Since $\tilde{\mathbf{A}}$ is the Fourier transform of a real-valued function and hence conjugate-symmetric in \mathbf{u} , we only estimate it on half the Nyquist region in order to avoid getting a singular covariance matrix. In the absence of pileup, we note that both $\bar{\mathbf{d}}^s$ and $\text{Cov}(\mathbf{d}^s)$, and therefore also the first term in (24), are proportional to the pre-patient photon flux, whereas the second term is independent of this quantity. As long as the photon fluence is high enough, we can

therefore approximate the second term with zero. We then obtain the Fisher information matrix $F_{\boldsymbol{\theta}}$ for $\boldsymbol{\theta}$ as:

$$F_{\boldsymbol{\theta}} \approx \left(\frac{\partial \bar{\mathbf{d}}^s}{\partial \boldsymbol{\theta}} \right)^{\top} \text{Cov}(\mathbf{d}^s)^{-1} \frac{\partial \bar{\mathbf{d}}^s}{\partial \boldsymbol{\theta}}. \quad (25)$$

To obtain the CRLB for the material decomposition $\tilde{\mathbf{A}}$ we introduce a change of variables by defining $\tilde{\mathbf{A}} = \left(\tilde{\mathbf{A}}, \tilde{\mathbf{A}}^* \right)^{\top} = \mathbf{T}\boldsymbol{\theta}$. Here \mathbf{T} is the block matrix⁴⁰ $\begin{pmatrix} \mathbf{I} & i\mathbf{I} \\ \mathbf{I} & -i\mathbf{I} \end{pmatrix}$, where \mathbf{I} is the identity matrix on the vector space on which $\text{Re } \tilde{\mathbf{A}}, \text{Im } \tilde{\mathbf{A}}$ are defined. As shown in appendix B, this gives the CRLB as

$$\text{Cov} \left(\hat{\tilde{\mathbf{A}}} \right)^{-1} \leq \mathbf{F}_{\tilde{\mathbf{A}}} = \begin{pmatrix} \mathbf{F}_{\tilde{\mathbf{A}}} & \mathbf{0} \\ \mathbf{0} & \mathbf{F}_{\tilde{\mathbf{A}}}^* \end{pmatrix}, \quad (26)$$

leading to $\text{Cov} \left(\hat{\tilde{\mathbf{A}}} \right) \geq \mathbf{F}_{\tilde{\mathbf{A}}}^{-1}$, for any unbiased estimator $\hat{\tilde{\mathbf{A}}}$ of $\tilde{\mathbf{A}}$. The components of $\mathbf{F}_{\tilde{\mathbf{A}}}$ are given by

$$(\mathbf{F}_{\tilde{\mathbf{A}}})_{l,l'}(\mathbf{u}, \mathbf{u}') = \frac{1}{\bar{q}^{\text{tot}2}} \frac{\partial \bar{q}^{\text{tot}}}{\partial A_l} \frac{\partial \bar{q}^{\text{tot}}}{\partial A_{l'}} \delta(\mathbf{u} - \mathbf{u}') \text{NEQ}_{l,l'}^{\mathcal{B}}(\mathbf{u}). \quad (27)$$

Since different spatial frequencies are independent, the Fisher information matrix $\mathbf{F}_{\tilde{\mathbf{A}}}$ is block diagonal and the block corresponding to spatial frequency \mathbf{u} is given by a rescaled version of $\text{NEQ}^{\mathcal{B}}(\mathbf{u})$, where \mathcal{B} is the set of basis functions in which $\tilde{\mathbf{A}}$ is expressed. $\mathbf{F}_{\tilde{\mathbf{A}}}$ can thus be inverted separately for each \mathbf{u} . This shows that $\text{NEQ}^{\mathcal{B}}(\mathbf{u})$, which describes performance for detection tasks, and $\mathbf{F}_{\tilde{\mathbf{A}}}^{-1}$, which describes the detector performance for material quantification tasks, are very closely related. Indeed, the Cramér-Rao lower bound can be expressed as

$$\text{Cov} \left(\hat{A}_l(\mathbf{u}), \hat{A}_{l'}(\mathbf{u}') \right) \geq \bar{q}^{\text{tot}2} \frac{[\text{NEQ}^{\mathcal{B}}(\mathbf{u})^{-1}]_{l,l'}}{\frac{\partial \bar{q}^{\text{tot}}}{\partial A_l} \frac{\partial \bar{q}^{\text{tot}}}{\partial A_{l'}}} \delta(\mathbf{u} - \mathbf{u}'). \quad (28)$$

In analogy with the definition (22) of DQE^{task} for a *detection* task we can define the DQE^{task} for *quantification* of basis material l as

$$\text{DQE}^{\text{task}}(\mathbf{u}) = \frac{\text{Var}(\hat{A}_l^{\text{ideal}})}{\text{Var}(\hat{A}_l(\mathbf{u}))}, \quad (29)$$

where $\text{Var} \left(\hat{A}_l^{\text{ideal}} \right)$ is the CRLB of the variance of \tilde{A}_l when measured with an ideal detector.

The estimated basis images are useful as they are, e.g. as a map of contrast agent distribution. However, it is also possible to make a frequency-dependent optimal weighted sum of the decomposed basis images, just as this can be done with the original energy bin images. The lower bound to the achievable variance in the basis images given by the CRLB translates to an upper bound of the achievable detectability in such a weighted basis image. This bound is given by the optimal-linear-observer detectability:³⁶

$$d'^2 \leq \Delta\theta^T F_\theta \Delta\theta = \frac{1}{4} \Delta\theta^T T^\dagger T F_\theta T^\dagger T \Delta\theta = \Delta\tilde{\mathbf{A}}^\dagger \mathbf{F}_{\tilde{\mathbf{A}}} \Delta\tilde{\mathbf{A}} = \Delta\tilde{\mathbf{A}}^\dagger \mathbf{F}_{\tilde{\mathbf{A}}} \Delta\tilde{\mathbf{A}} + \Delta\tilde{\mathbf{A}}^T \mathbf{F}_{\tilde{\mathbf{A}}}^* \Delta\tilde{\mathbf{A}}^*. \quad (30)$$

The block-diagonality of the Fisher information matrix allows us to treat spatial frequency components independently, the first term in this sum is an integral over the half-plane $u > 0$. Since $\Delta\tilde{A}_l(\mathbf{u})$ and $\text{NEQ}^B(\mathbf{u})$ are both conjugate-symmetric, this allows us to extend the integral to the entire \mathbf{u} plane:

$$d'^2 \leq \frac{1}{\bar{q}^{\text{tot}2}} \int_{\mathbb{R}^2} \sum_l \sum_{l'} \frac{\partial \bar{q}^{\text{tot}}}{\partial A_l} \Delta\tilde{A}_l(\mathbf{u})^\dagger [\text{NEQ}^B(\mathbf{u})]_{l,l'} \Delta\tilde{A}_{l'}(\mathbf{u}) \frac{\partial \bar{q}^{\text{tot}}}{\partial A_{l'}} d\mathbf{u} = \int_{\mathbb{R}^2} \Delta\mathbf{S}^B(\mathbf{u})^\dagger \text{NEQ}^B(\mathbf{u}) \Delta\mathbf{S}^B(\mathbf{u}) d\mathbf{u}. \quad (31)$$

By comparing (30) with (18), we see that the same detectability is obtained by combining the different basis images as from combining the original energy bin images, as long enough statistics is available that the estimator variance will be close to the CRLB. This is a generalization of the analogous result for zero frequency derived by Alvarez.⁴¹

Another way to combine the basis images is to generate a synthetic monoenergetic image^{42,43} as $p^{\text{mono}}(E) = \sum_{l=1}^{N_m} A_l(\mathbf{r}) f_l(E)$. This is useful because the image values are easy to interpret. Note, however, that the basis images in this case are combined using frequency-independent weight functions, meaning that there is no guarantee that there is an energy for which the resulting monoenergetic image has optimal detectability.

III. MATERIALS AND METHODS

To illustrate the matrix-valued NEQ and DQE measures, we will study their form for two simple models (one modeling K-escape and one modeling Compton scatter in the detector), and also for a more realistic simulation model of a CdTe detector.

III.A. Fluorescence model

As a simplified model of fluorescence K-escape, we assume that an incident photon of energy E will deposit either its entire energy, with probability $1 - p_F(E)$, or an energy $E - E_F$ with probability $p_F(E)$. E_F is thus the energy of the fluorescence photon, and the probability of fluorescence escape $p_F(E)$ is a function of E with $p_F(E) = 0$ for $E \leq E_F$. For simplicity, we neglect detection of secondary (fluorescence) photons in other detector elements, e.g. the detector is assumed to have coincidence logic that eliminates secondary events but is not able to reconstruct the original photon energies. We also assume that the detector has infinitely many bins, infinitely small pixels and perfect energy resolution, i.e. the fluorescence escape is the only degrading factor. The transfer function is then $H(\mathbf{u}, E, \varepsilon) = (1 - p_F(E))\delta(E - \varepsilon) + p_F(E)\delta(E - E_F - \varepsilon)$ and an incident spectrum $\bar{q}(E)$ results in a measured spectrum $\bar{d}(\varepsilon) = (1 - p(\varepsilon))\bar{q}(\varepsilon) + p(\varepsilon + E_F)\bar{q}(\varepsilon + E_F)$. Since each photon is only registered once, the measurements at different energies are independent random variables, and the cross-spectral density is given by $W(\mathbf{u}, \varepsilon, \varepsilon') = \bar{d}(\varepsilon)\delta(\varepsilon - \varepsilon')$. Inserting these results into (9) gives, after some algebra,

$$\begin{aligned} \text{NEQ}(\mathbf{u}, E, E') = & \left[\frac{(1 - p_F(E))^2}{\bar{d}(E)} + \frac{p_F(E)^2}{\bar{d}(E - E_F)} \right] \bar{q}(E)^2 \delta(E - E') + \\ & \frac{(1 - p_F(E))\bar{q}(E)p_F(E')\bar{q}(E')}{\bar{d}(E)} \delta(E' - (E + E_F)) + \\ & \frac{p_F(E)\bar{q}(E)(1 - p_F(E'))\bar{q}(E')}{\bar{d}(E')} \delta(E' - (E - E_F)). \end{aligned} \quad (32)$$

The DQE can then be obtained from (13).

To plot the DQE matrix for a simple example, we discretized energy in steps of 1 keV and assumed $E_F = 25$ keV and $p_F(E) = 0.2$ (independent of E) for $E > E_F$. For simplicity we also assumed a rectangular incident spectrum: $q(E) = \bar{q}^0 = \bar{q}^{\text{tot}}/(E_2 - E_1)$ for $E_1 < E < E_2$ and 0 otherwise. In order to study the effect of spectral overlap, we studied two different incident spectra: one that is nonzero between $E_1 = 40$ keV and $E_2 = 60$ keV, which gives nonoverlapping deposited spectra for the K-escape peak and photopeak events, and one that is nonzero between $E_1 = 40$ keV and $E_2 = 120$ keV, which produces overlap between the photopeak and K-escape spectra. We also used (22) to calculate DQE^{task} for different task functions $\Delta S(E)$ which were, for simplicity, taken to be piecewise constant, equal to either

0 or $\pm\Delta S_0$, as described below.

III.B. Scatter model

In order to demonstrate how the proposed framework treats interactions where the energy information is lost, we also studied a simple model for Compton scatter in the detector. In this model, we assume that an incident photon is either photoabsorbed with probability $1 - p_S$, depositing all its energy, or Compton scattered with probability $p_S = 0.5$. In the latter case it deposits an energy E_S which we for simplicity assume to be fixed at 10 keV independent of the incident energy. We also assume that all scattered photons are stopped by blocking lamellae or escape from the detector, so that each photon is counted only once. Like in the fluorescence model, we assumed that the incident spectrum is constant, equal to $\bar{q}^0 = \bar{q}^{\text{tot}}/(E_2 - E_1)$ between $E_1 = 40$ keV and $E_2 = 120$ keV and 0 otherwise. Once again, the photopeak and distorted spectra do not overlap. The detected spectrum $\bar{d}(\varepsilon) = p_S \bar{q}^{\text{tot}} \delta(E - E_S) + (1 - p_S) \bar{q}(E)$ and, after some calculations, $\text{DQE}(E, E') = \frac{p_S}{E_1 - E_2} + (1 - p_S) \delta(E - E')$.

III.C. CdTe simulation

To study a more realistic case, we used Monte Carlo simulation (pyPENELOPE⁴⁴, based on PENELOPE⁴⁵) to model a CdTe detector. A special version was compiled in order to include secondary photons. For each 1 keV-step from 1 to 120 keV, a pencil beam of photons incident on a 3 mm thick slab of CdTe was simulated, and the location and energy of each photon interaction was recorded. Care was taken to avoid double-counting energy released as K-escape photons.

We simulated charge sharing according to the uniform spherical charge cloud model of Taguchi²⁶, where the diameter d of the charge cloud is related to the deposited energy E as $d = d_0(E/E_{\text{ref}})^{1/3}$, and we used $d_0 = 30 \mu\text{m}$ at $E_{\text{ref}} = 70$ keV. By dividing the detector into $0.5 \times 0.5 \text{ mm}^2$ pixels and calculating the charge cloud volume fraction located within the borders of each pixel, we obtained the total charge collected in each pixel. The charge contributions from all interactions stemming from each individual photon were then summed, and the total number of registered photons in each of five energy bins (25-40, 41-54, 55-64, 65-77 and 78-120 keV) were recorded. We repeated this for a grid of 16×16 positions of

the pencil beam in one quadrant of the detector cell, extending from the center to the pixel border in the positive x and y directions. Exploiting mirror symmetry in two dimensions, we obtained the point-spread function $h_k(\Delta\mathbf{r}, E)$ on a grid with 30×30 sample points for each detector cell in a grid of 3×3 cells. The point-spread function was also symmetrized with respect to interchanging the x and y coordinates.

To obtain the autocovariance function, we used the same pencil beam simulation but with a randomized position of each incident photon to simulate homogeneous illumination of the center pixel. For each incident energy E , we recorded the number of incident photons $N_{\mathbf{n},k,\mathbf{n}',k'}(E)$ leading to a registered count in both energy bin k of pixel \mathbf{n} and energy bin k' of pixel $\mathbf{n}' = \mathbf{n} + \Delta\mathbf{n}$. The covariance of the number of registered photons $N_{\mathbf{n},k}(E)$ and $N_{\mathbf{n}',k'}(E)$ in these two pixel-bin pairs is given by $\text{Cov}(N_{\mathbf{n},k}(E), N_{\mathbf{n}',k'}(E)) = N_{\mathbf{n},k,\mathbf{n}',k'}(E)$, since the photons registered in either of $N_{\mathbf{n},k}(E)$ and $N_{\mathbf{n}',k'}(E)$, but in not both, are independent between these two measurements. By summing over \mathbf{n} in the grid of 3×3 detector cells, we simulated homogeneous illumination of the entire pixel array and thereby obtained the autocovariance function $K_{\Delta\mathbf{n},k,k'}^s(E)$ for each incident energy E . $K_{\Delta\mathbf{n},k,k'}^s(E)$ was calculated for $-1 \leq n_x, n_y \leq 1$, i.e. only correlations between nearest neighbors was taken into account. We symmetrized the autocovariance function using mirror symmetry in x and y and with respect to interchanging the x and y coordinates.

We used discrete Fourier transformation to calculate the transfer function $H_k(\mathbf{u}, E)$ and energy-dependent cross-spectral density $W_{k,k'}^s(\mathbf{u}, E)$. We then calculated the noise cross-spectral density of the bin counts $W_{k,k'}^s(\mathbf{u})$ by combining contributions from different energies using a 120 kVp tungsten anode X-ray spectrum with a prepatient photon fluence of $4 \cdot 10^6 \text{ mm}^{-2}$ and 12° anode angle, filtered through 2.5 mm Al (prepatient filtration) and 100 mm water.⁴⁶ The spectrum was obtained from Spektr 3.0⁴⁷ and the linear attenuation coefficients were obtained from NIST⁴⁸. Electronic noise and pileup were not included in the simulation. The NEQ and DQE matrices were calculated in the basis of monoenergies using Eqs. 9 and 13 and in the basis $\mathcal{B} = \{\text{Water, Bone}\}$ using Eqs. 20 and 21. By calculating the eigenvalues of $\text{NEQ}^{\mathcal{B},\text{ideal}}(\mathbf{u})^\dagger^{-1/2} \text{NEQ}^{\mathcal{B}}(\mathbf{u}) \text{NEQ}^{\mathcal{B},\text{ideal}}(\mathbf{u})^{-1/2}$, we obtained the the maximum and minimum DQE^{task} for any detection task. We also calculated the task-specific DQEs for quantifying the amount of cortical bone and water in a two-basis decomposition using Eqs. 28 and 29.

IV. RESULTS

IV.A. Fluorescence model

The results for the fluorescence model are shown in Fig. 1, in Fig. 1(a-c) for the nonoverlapping spectrum case and in Fig. 1(d-i) for the overlapping spectrum case. In Fig. 1(c,f-i), different task functions are shown together with the diagonal of the DQE matrix and the corresponding DQE^{task} values. The DQE matrix was discretized by replacing the delta function with a square of width 1 keV. For the overlapping spectrum case (Fig. 1e), the delta function coefficients in the DQE matrix are 0.68 – 0.84 on the diagonal and 0.16 on the off-diagonal lines.

IV.B. Scatter model

The results for the Compton scatter model are shown in Fig. 2. Fig. 2(a) shows the incident and deposited spectra. The DQE matrix was discretized by replacing the delta function with a square of width 1 keV. Fig. 2(c-d) show task functions for (c) density imaging and (d) spectral imaging, together with the diagonal of the DQE matrix and the resulting DQE^{task} .

IV.C. CdTe simulation

Fig. 3 shows the simulated point-spread functions for the CdTe model for monochromatic beams of 40, 70 and 100 keV. The corresponding transfer functions $H_k(\mathbf{u}, E)$ are shown in Fig. 4 for \mathbf{u} ranging from $u = 0 \text{ mm}^{-1}$ to three times the Nyquist frequency. The matrix elements of the cross-spectral density are shown as a function of frequency in Fig. 5, for u from 0 mm^{-1} to the Nyquist frequency. Since the autocorrelation function is mirror-symmetric in this model, the cross-spectral density is also symmetric, i.e. extends by mirroring in zero and in the Nyquist frequency.

The zero-frequency NEQ and DQE matrices in the basis of monoenergies are displayed in Fig. 6 together with plots of their respective diagonals. Fig. 7(a) shows the components of the $\text{NEQ}^{\mathcal{B}}$ matrix for the CdTe model and for an ideal detector, as a function of spatial frequency for basis materials water and bone. The unattenuated photon fluence of $4 \cdot$

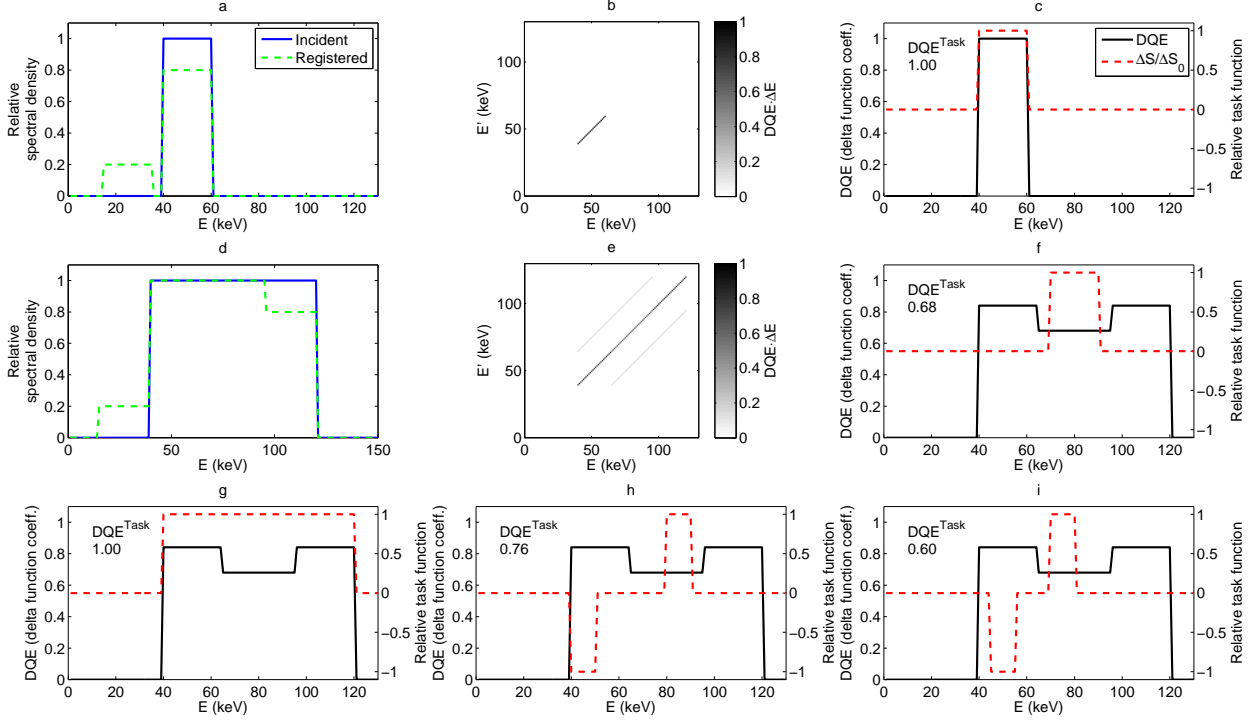


FIG. 1 Results for the fluorescence model. (a) Incident and deposited spectra in the nonoverlapping spectrum case, discretized with $\Delta E = 1$ keV. (b) DQE matrix in the nonoverlapping spectrum case. (c) diagonal of the DQE matrix together with the task function and DQE^{task} for a density imaging task in the nonoverlapping spectrum case. (d) Incident and deposited spectra in the overlapping spectrum case. (e) DQE matrix in the overlapping spectrum case. (f-i) Diagonal of the DQE matrix in the overlapping spectrum case, together with task function and DQE^{task} for four different tasks: (f) nonoverlapping density imaging task; (g) overlapping density imaging task; (h) nonoverlapping spectral imaging task; and (i) overlapping spectral imaging task. Since DQE is singular, the plotted DQE curves in (c,f-i) show the coefficient in front of $\delta(E - E')$.

10^6 mm^{-2} before the object gives $4.35 \cdot 10^5 \text{ mm}^{-2}$ after the object. The corresponding DQE^{B} is shown for the same basis functions in Fig. 7(b), whereas Fig. 7(c) shows the largest and smallest DQE^{task} for any detection task. Finally, Fig. 7(d) shows DQE^{task} for quantifying water and bone in a two-material decomposition, calculated with Eq. 29.

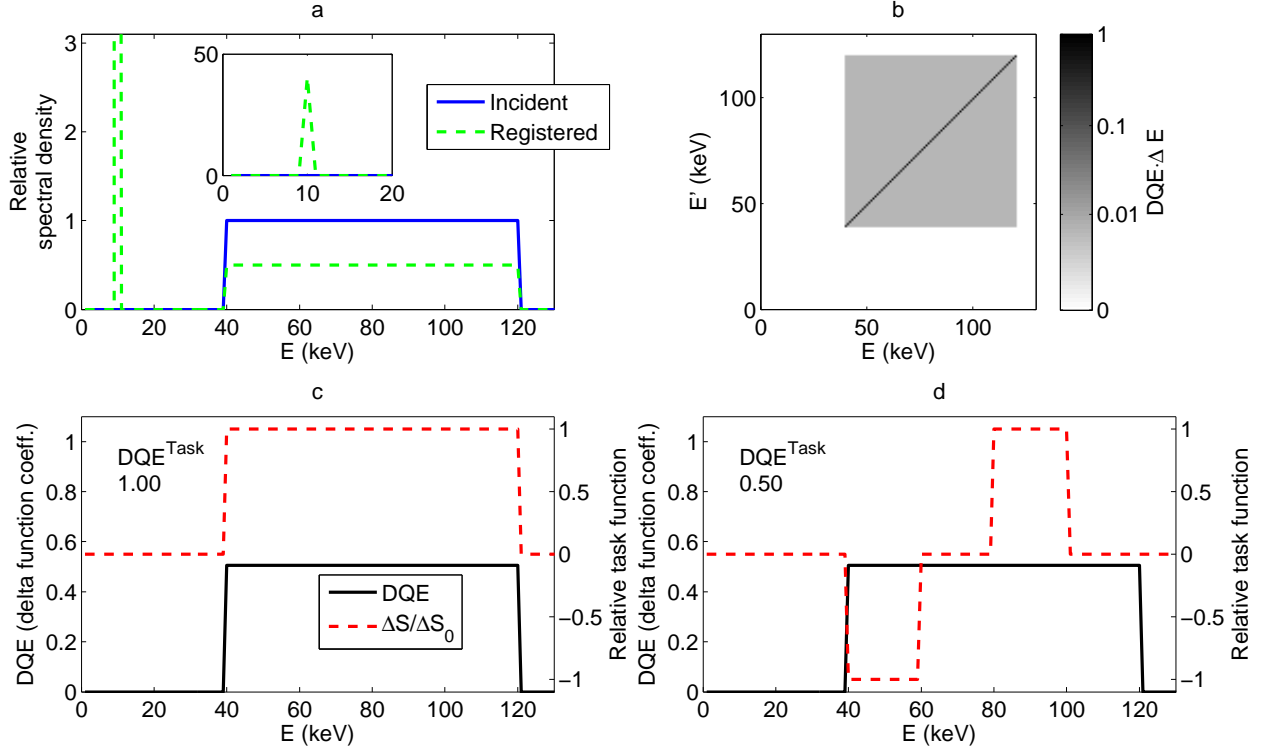


FIG. 2 Results for the scatter model. (a) Incident and deposited spectra. Insert: zoomed-out view showing the Compton peak. (b) DQE matrix, discretized with $\Delta E = 1$ keV. Note that the color scale is logarithmic, to visualize the low-intensity background of $6.2 \cdot 10^{-3} \text{ keV}^{-1}$. (c) diagonal of the DQE matrix together with the task function and DQE^{task} for a density imaging task. (d) diagonal of the DQE matrix together with the task function and DQE^{task} for a spectral imaging task. Since DQE is singular, the plotted DQE curves in (c-d) show the coefficient in front of $\delta(E - E')$.

V. DISCUSSION

V.A. Fluorescence model

In the simple fluorescence model, the NEQ matrix (32) and the corresponding DQE matrix are independent of spatial frequency, nonzero along the diagonal for the energies contained in the measured spectrum and, if there is spectral overlap, along two off-diagonal lines (Fig. 1(b,e)). To interpret this result, note that according to Eq. 10 the detectability of a feature with differential signal $\Delta S(\mathbf{u}, E)$ at frequency (\mathbf{u}) is obtained as a sum of contributions $\Delta S(\mathbf{u}, E) \cdot \text{NEQ}(\mathbf{u}, E, E') \cdot \Delta S(\mathbf{u}, E')$ from all *pairs* of energies E, E' . The first term of (32), which contains the diagonal elements of the matrix, shows that a relative signal

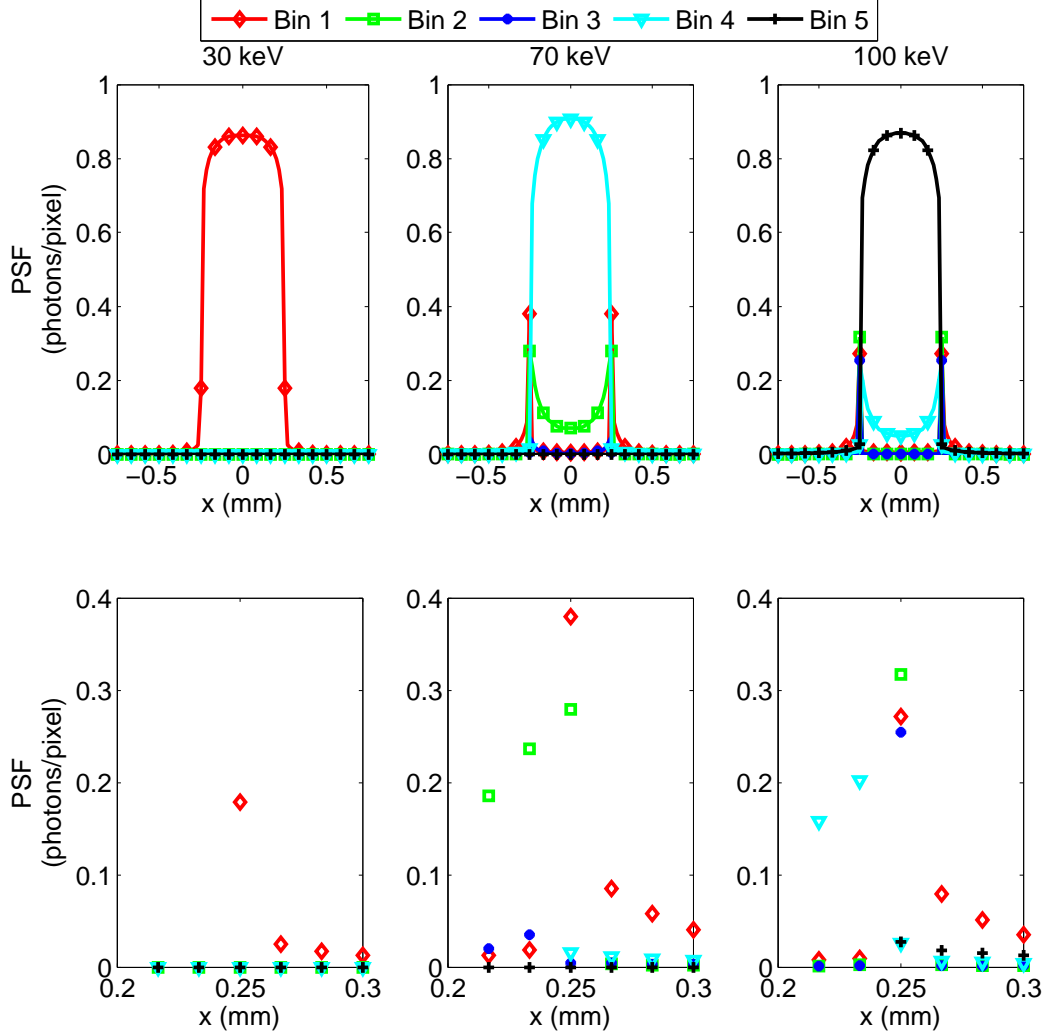


FIG. 3 Slices along the x axis of the simulated energy-bin point-spread functions in the CdTe model measured as photons per pixel, $x_0 y_0 h_k(\Delta \mathbf{r}, E)$, for three incident monoenergies: 30, 70 and 100 keV. The lower row contains close-ups of the region closest to the pixel border. (In the lower row, the data points are not connected by lines since the psf is not expected to be smooth.)

difference at energy E contributes to d'^2 with two terms. The first term is the contribution from the non-fluorescence (photopeak) interactions at energy E and the second term is the contribution from the fluorescence interactions with original energy E and registered energy $E - E_F$. The two off-diagonal contributions in (32) are nonzero only for $E' = E + E_F$ and $E' = E - E_F$, respectively. These terms contain the contribution from overlap between the photopeak and the K-escape peak. The denominator for each of these contributions is the quantum noise variance, equal to the number of registered events at the deposited energy.

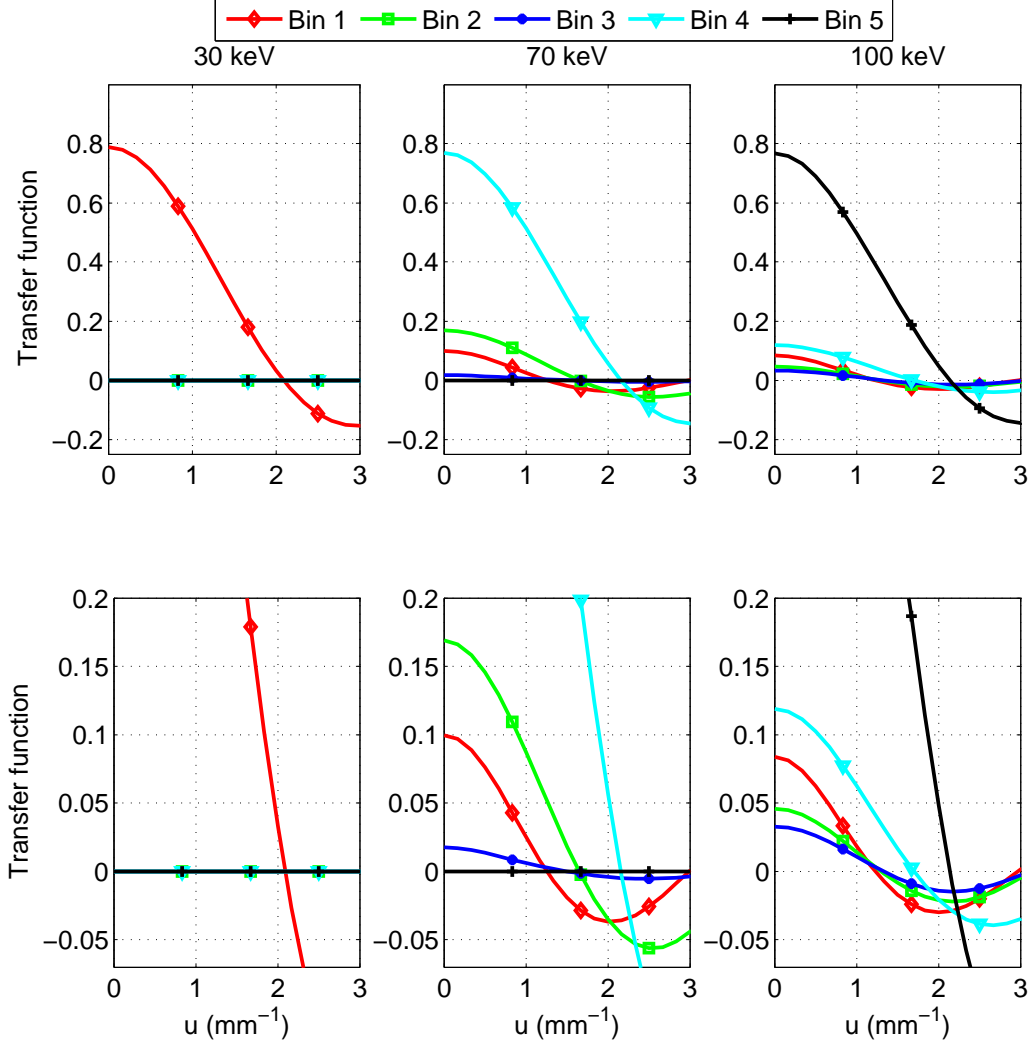


FIG. 4 Transfer functions $H_k(\mathbf{u}, E)$ in the CdTe model for three incident monoenergies: 30, 70 and 100 keV. These are plotted along the positive u axis up to three times the Nyquist frequency 1 mm^{-1} . The lower row contains close-up views of the upper plots.

When the incident spectrum is narrow enough that the photopeak and K-escape spectra do not overlap (Fig. 1(a-c)), there are no off-diagonal terms and the DQE matrix is a delta function along the diagonal with a coefficient of 1. Even though the K-escape photons are registered with the wrong energy, there is no risk that these will be confused with photopeak photons, and since there is no ambiguity about the true energy, the K-escape photons do not cause any performance degradation at all and the DQE^{task} for any imaging task is 1.

When the spectrum is broad enough to give overlap between the photopeak and K-escape events, on the other hand, off-diagonal elements appear in the DQE matrix and the values

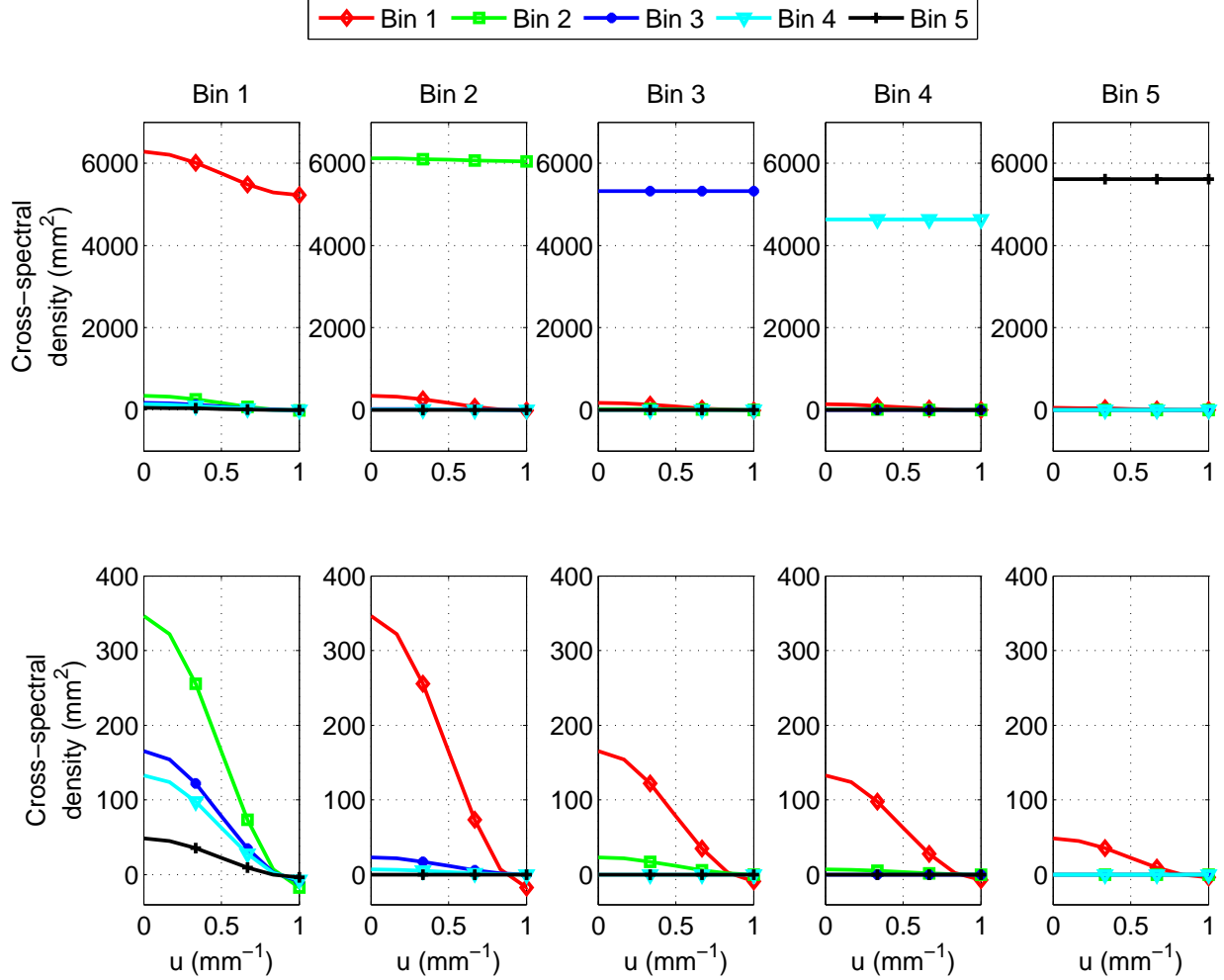


FIG. 5 Cross-spectral density $x_0^2 y_0^2 (W_{d^+})_{kk'}(\mathbf{u})$ in the CdTe model for broad-spectrum illumination, along the positive u axis up to the Nyquist frequency (1 mm^{-1}). Each column of plots represents one k and each curve one k' . The lower row contains close-up views of the upper plots. Note that each cross-term is plotted twice since $(W_{d^+})_{kk'}(\mathbf{u})$ is symmetric in k and k' .

of the diagonal elements decrease (Fig. 1(d-i)). The diagonal elements of the DQE matrix indicate how much $\Delta S(\mathbf{u}, E)$ at each energy E alone contribute to the total d'^2 , regardless of what other energies are present in $\Delta S(\mathbf{u}, E)$. In this case, the diagonal DQE elements are highest near the maximum energy, where the recorded spectrum does not include any K-escape component, and near the minimum energy, where the K-escape events from these photons are registered below the minimum incident energy and do not have to compete with the noise from photopeak events.

The off-diagonal terms, on the other hand, specify the contribution to d'^2 caused by the

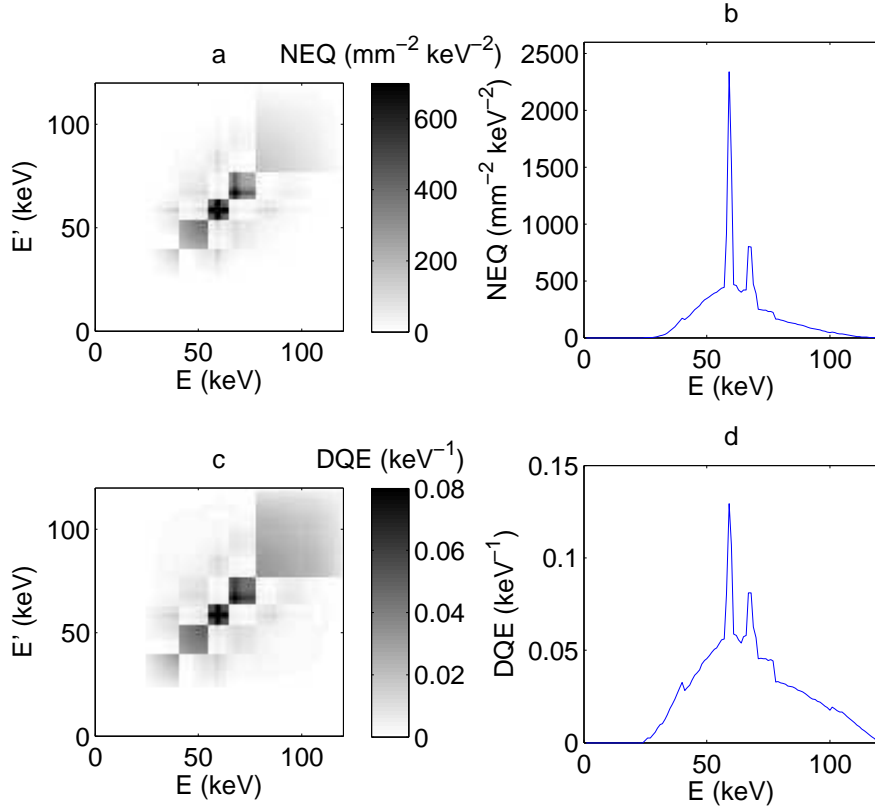


FIG. 6 (a) Zero-frequency NEQ matrix for the CdTe model. (b) Diagonal elements of the NEQ matrix in (a). (c) Zero-frequency NEQ matrix for the CdTe model. (d) Diagonal elements of the DQE matrix in (c).

presence of a signal at both energy E and E' . This contribution can be either positive or negative depending on the task. Since the off-diagonal terms are positive in this model, the detectability increases if ΔS has the same sign at both energies and decreases if ΔS has opposite signs at the two energies. A case when ΔS has the same sign at E and E' can correspond e.g. to a density imaging task, where the total number of registered photons is more important than the energy distribution. In this case the simultaneous presence of photons at both energies in ΔS is actually beneficial, since the d'^2 contribution is proportional to the square of the differential signal, and increasing spectral overlap in the signal (while keeping the background noise fixed) helps concentrate more signal at a single measurement energy. On the other hand, a case where ΔS has opposite signs at the two energies is a material discrimination task, e.g. K-edge imaging. Here, the simultaneous presence of energies E and E' decreases the detectability since spectral overlap degrades the

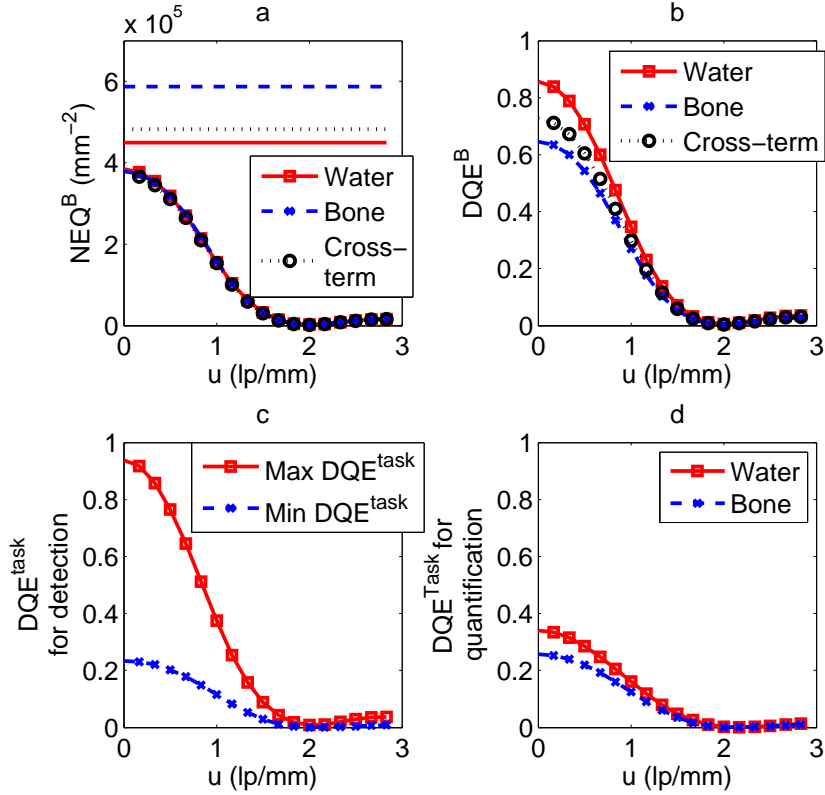


FIG. 7 (a) Components of the $\text{NEQ}^{\mathcal{B}}$ matrix with water and bone as basis functions. The plots with markers apply to the CdTe simulation model whereas the plots without markers are the corresponding values for an ideal detector. (b) Components of the $\text{DQE}^{\mathcal{B}}$ matrix for the CdTe simulation model with water and bone as basis functions. (c) Maximum and minimum DQE^{task} for any detection task, for the CdTe model. (d) DQE^{task} for quantifying the amount of water and bone, respectively, in a two-basis decomposition with the CdTe model.

ability of the detector to measure true spectral differences.

In the model studied here, the off-diagonal terms are nonzero only for $E - E' = E_F$. The impact of the fluorescence on detectability is therefore dependent on whether the task function $\Delta S(\mathbf{u}, E)$ involves energies with spectral overlap or not. This is demonstrated in Fig. 1(f-i). When the task is to detect a signal difference in a narrow energy band, the DQE^{task} is simply given by the diagonal value of the DQE matrix for that energy range (Fig. 1(f)). This is less than unity because the registered change in photon flux must be detected in the presence of a larger noise contribution from co-registered K-escape and photopeak events. On the other hand, when the task is to detect a signal difference across a broad

range of energies, the off-diagonal elements cause constructive interference and $\text{DQE}^{\text{task}} = 1$, as for an ideal detector (Fig. 1(g)). For a density imaging task, the off-diagonal elements thus improve DQE^{task} .

For a spectral imaging task, i.e. when trying to detect an attenuation difference between two energy bands, the off-diagonal elements have a different effect (Fig. 1(h-i)). For a spectral task where the spectral bands do not have any overlap due to fluorescence, DQE^{task} is given by the average over the two energy bands of the delta function coefficient along the diagonal of DQE, i.e. the off-diagonal elements do not affect the result. If the bands are positioned so that K-escape events from one of them overlaps with photopeak events from the other, the off-diagonal elements give negative interference and decrease DQE^{task} . In this case, the off-diagonal elements are detrimental, since cross-talk from one energy band to the other makes it more difficult to detect a spectral difference.

V.B. Scatter model

In the Compton scatter model (Fig. 2) half the incident spectrum is registered at its correct energy, while half is registered as a peak at 10 keV (Fig. 2(a)) This is reflected in the form of the DQE matrix (Fig. 2(b)), which is the sum of two contributions. The photoelectric interactions give a diagonal with delta functions whose coefficient is 0.5, i.e. half the DQE of an ideal detector. The Compton interactions provide information that a photon was detected but do not contain any energy information. Their contribution is evenly distributed as a weak background over the entire square formed by the spectral supports of $\bar{q}(E)$ and $q(E')$. The total area of the diagonal line and the background is the same since each of them are generated from 50% of the photons.

For a density imaging task where ΔS is constant as a function of energy, d'^2 is given by the integral over nonzero part of the DQE matrix, so that the two contributions add and give $\text{DQE}^{\text{task}} = 1$. Since only the total number of registered photons matters in this case, the fact that some of them are registered at the wrong energy does not degrade the performance. For a spectral imaging task on the other hand, the detectability is obtained as an integral of the NEQ over four squares in the (E, E') diagram, two near the diagonal with positive sign and two away from the diagonal with negative sign. The uniform background term in the NEQ matrix therefore gives a net contribution of 0, so that $\text{DQE}^{\text{task}} = 0.5$, reflecting

only the photoelectric contribution. The Compton events, which are all registered with the same energy, thus contain as much information as photoelectric events for density imaging tasks but no information at all for a pure spectral task. A real-world imaging task will typically be an intermediate between these two types, meaning that the Compton events will contribute some information but less than the photoelectric events. Also note that this model is simplified in the sense that, in a real detector, the deposited energy from a Compton interaction is random with a distribution function that depends on the incident energy and the scattering angle, meaning that the Compton interactions do contain some energy information.

V.C. CdTe simulation

As shown in Fig. 3, the point-spread function $h_k(\Delta\mathbf{r}, E)$ of the CdTe simulation model depends on the incident energy. When a monoenergetic beam impinges on the interior of a pixel, the majority of counts are registered in the energy bin that includes the true energy: bin 1, 4 and 5 for 30, 70 and 100 keV, respectively. For a 30 keV beam, nothing is registered in the other bins, since pileup is not included in the model and the energies of different photons thus cannot be added together. For higher incident energies, some photons are misregistered in lower energy bins due to charge sharing and fluorescence. For example, a 100 keV beam incident precisely on the border between two pixels will be registered in energy bin 2 (41-54 keV) since only about half the photon energy, 50 keV, is deposited in the studied pixel. If the same beam hits inside the pixel but close to the border, a fraction (up to 20%) of the photons are registered in bin 4 (65-77 keV) since they only lose a minor part of their energy to charge sharing or fluorescence. Finally, just outside the pixel border, the majority of the events are registered in energy bin 1 (25-40 keV) since most of the energy of these photons is deposited in the neighboring pixel.

The shape of the point-spread function is reflected in the transfer function $H_k(\mathbf{u}, E)$ (Fig. 4). In each case, the transfer function for the energy bin encompassing the incident energy falls off from a zero-frequency value close to 0.8, signifying that about 80% of the total number of photons are registered in that energy bin, and crosses 0 near twice the Nyquist frequency, reflecting the nearly rectangular point-spread function. The other energy bins detect smaller fractions of the photons and fall off more rapidly, indicating that the blurring

from the inter-pixel cross-talk suppresses high spatial frequencies.

The low-pass character of the cross-talk can also be seen from the cross-spectral density plotted in Fig. 5. As seen in these figures, the diagonal elements of W_{d+} are nearly constant functions of spatial frequency, which indicates that the noise in these is uncorrelated between pixels. The exception is the lowest energy bin, which has a low-frequency component in its noise stemming from the fact that some photons are counted in this energy bin in more than one pixel. The cross-elements of W_{d+} exhibit strong low-frequency correlations since photons are typically registered in one energy bin in the pixel of incidence and in another energy bin in a neighboring pixel. The strongest such correlation is found between energy bins 1 and 2. This shows that the correlation structure in the measured image requires a joint description in terms of both spatial and energy correlations.

The zero-frequency NEQ and DQE matrices in the basis of monoenergies (Fig. 6) exhibit a block-like structure with the block borders corresponding to the energy thresholds. These plots show that the largest cross-terms, and thereby the strongest coupling between different energies, is found within each energy bin, i.e. in the diagonal blocks. Note that the relative intensity of the blocks resembles the three diagonal bands caused by the loss of a fixed amount of energy in the simplified fluorescence model (Fig. 1(e)). Figs 6(b,d) also show that both the NEQ and DQE are largest for the energies corresponding to the characteristic X-ray peaks in the spectrum. All energies falling within a certain energy bin are detected against the same amount of background noise, and since the detectability is a quadratic function of the signal difference, a certain relative signal difference ΔS gives a larger detectability when the spectral density is higher. It is therefore easier to detect an attenuation difference right at a characteristic X-ray energy of the source than at a neighboring energy. This also explains why the matrix-valued DQE is dependent on the X-ray spectrum shape.

The $\text{NEQ}^{\mathcal{B}}$ and $\text{DQE}^{\mathcal{B}}$ are plotted as functions of spatial frequency in Fig. 7(a-b). Note that the NEQ values for the ideal detector are slightly higher than the transmitted photon fluence of $4.35 \cdot 10^5 \text{ mm}^{-2}$, in particular for bone, reflecting the higher detectability of an ideal energy-resolving detector compared to an ideal photon-counting detector with no energy discrimination. The task-specific DQE values for detecting water and bone are obtained directly from Fig. 7(b) as the diagonal elements of the $\text{DQE}^{\mathcal{B}}$ matrix. The plots show that the performance for both detection of bone and soft tissue suffer relatively little from the degraded energy resolution caused by charge sharing and fluorescence, since the zero-

frequency DQE^{task} is 0.86 for water and 0.65 for bone. The sinc-like decrease towards higher frequencies is caused by the pixel aperture. The cross-term is positive, meaning that the presence of both soft tissue and bone in a detection task will cause constructive interference, i.e. increase detectability.

The maximum DQE^{task} for any imaging task is 0.94, while the minimum is 0.23 (Fig. 7(c)). Both water and bone detection are therefore tasks for which the performance of the studied detector comes relatively close to the maximum. For material quantification, on the other hand, the DQE^{task} is severely degraded by the imperfect energy resolution of the detector (0.34 for water and 0.26 for bone) and comes close to its lowest possible value for any detection task. (Fig. 7(d)). Thus, the mis-registration of photon energies has a limited effect on detecting a small change in the amount of water or bone, since this also affects the total number of photons, but a large effect on the ability to determine what material caused a loss of flux, which requires good energy resolution.

In the model studied here, we have neglected electronic noise for the purpose of making the effects of the spectrum shape and nonideal energy response stand out clearly. In a real detector, electronic noise will blur the detected spectrum, so that the transition of the point-spread function at the pixel border becomes smoother compared to Fig. 3 and the characteristic X-rays are less prominent in the NEQ matrix compared to Fig. 6.

VI. CONCLUSION

In this work, we have shown how the framework of linear-systems theory can be extended to describe energy-resolving detectors. We have demonstrated a natural way of generalizing the NEQ and DQE metrics to matrix-valued quantities containing information about both the spatial resolution, detection efficiency and energy resolution of the detector. Furthermore, we have demonstrated how basis material decomposition can be used to express these matrices in a compact form and that they are closely related to the Cramér-Rao lower bound which describes the detector performance for material decomposition. We have thus merged two approaches for detector performance assessment, the linear-systems framework for describing detection task performance and the CRLB approach for describing material decomposition performance.

The ideal-linear-observer performance derived here may not always mimic the perfor-

mance of a human observer. However, if the measured count numbers are large enough to be described by Gaussian statistics, the optimal-linear-observer performance equals the performance of the ideal observer³⁶ and therefore gives an approximate upper limit to the detection performance achievable with advanced image processing.

Although photon-counting detectors have been studied in the examples presented here, the proposed framework can also be extended to other spectral imaging systems, such as dual-layer detectors. Future work should also include pileup and electronic noise. Another topic for future work is to develop methods for measuring the matrix-valued NEQ and DQE experimentally, for detector modules and for complete imaging systems. This new framework for detector performance characterization will help the development of photon-counting X-ray imaging systems by facilitating comparisons between different detector designs and elucidating the trade-off between different parameters, such as spatial resolution, energy resolution and dose efficiency.

ACKNOWLEDGMENTS

This study was supported by NIH Grant U01 EB01714003. The authors would like to thank Moa Yveborg and Jesse Tanguay for helpful discussions.

DISCLOSURE OF CONFLICTS OF INTEREST

Mats Persson is stockholder of and consultant for Prismatic Sensors AB. Norbert J. Pelc is consultant for Prismatic Sensors AB.

Appendix A: Fourier-domain covariance matrix

In this section we derive the Fourier-domain expression for the optimal-linear-observer detectability. The matrix elements of the discrete-space Fourier operator and its inverse is $(\mathcal{F}_{\text{DS}})_{\mathbf{n}}(\mathbf{u}) = e^{-2\pi i \mathbf{u} \cdot \mathbf{r}_{\mathbf{n}}}$ and $(\mathcal{F}_{\text{DS}}^{-1})_{\mathbf{n}}(\mathbf{u}) = \Delta_x \Delta_y e^{2\pi i \mathbf{u} \cdot \mathbf{r}_{\mathbf{n}}}$. Eq. 6 then gives

$$\begin{aligned} d'^2 &= \left(\mathcal{F}_{\text{DS}} \Delta \bar{\mathbf{d}}^s \right)^\dagger \left(\mathcal{F}_{\text{DS}}^\dagger \right)^{-1} \text{Cov}(\mathbf{d}^s)^{-1} \mathcal{F}_{\text{DS}}^{-1} \mathcal{F}_{\text{DS}} \Delta \bar{\mathbf{d}}^s \\ &= (\Delta \bar{\mathbf{D}}^s)^\dagger \left(\mathcal{F}_{\text{DS}} \text{Cov}(\mathbf{d}^s) \mathcal{F}_{\text{DS}}^\dagger \right)^{-1} \Delta \bar{\mathbf{D}}^s, \end{aligned} \tag{A1}$$

where \dagger denotes conjugate-transpose. Since \mathbf{d}^s is wide-sense stationary,

$$\begin{aligned}
\left[\mathcal{F}_{\text{DS}} \text{Cov}(\mathbf{d}^s) \mathcal{F}_{\text{DS}}^\dagger \right]_{k,k'}(\mathbf{u}, \mathbf{u}') &= \sum_{\mathbf{n}=-\infty}^{\infty} \sum_{\mathbf{n}'=-\infty}^{\infty} \text{Cov}(d_{\mathbf{n},k}^s, d_{\mathbf{n}',k'}^s) e^{2\pi i(-\mathbf{u}\cdot\mathbf{r}_{\mathbf{n}} + \mathbf{u}'\cdot\mathbf{r}_{\mathbf{n}'})} \\
&= \sum_{\mathbf{n}=-\infty}^{\infty} \sum_{\Delta\mathbf{n}=-\infty}^{\infty} K_{\Delta\mathbf{n},k,k'}^s e^{2\pi i((\mathbf{u}'-\mathbf{u})\cdot\mathbf{r}_{\mathbf{n}} + \mathbf{u}'\cdot\Delta\mathbf{r}_{\mathbf{n}})} = \sum_{\mathbf{n}=-\infty}^{\infty} e^{2\pi i(\mathbf{u}'-\mathbf{u})\cdot\mathbf{r}_{\mathbf{n}}} \sum_{\Delta\mathbf{n}=-\infty}^{\infty} K_{\Delta\mathbf{n},k,k'}^s e^{2\pi i\mathbf{u}'\cdot\Delta\mathbf{r}_{\mathbf{n}}} \\
&= \sum_{\mathbf{n}=-\infty}^{\infty} e^{2\pi i(\mathbf{u}'-\mathbf{u})\cdot\mathbf{r}_{\mathbf{n}}} W_{k,k'}^s(-\mathbf{u}') = \frac{1}{\Delta_x \Delta_y} \delta(\mathbf{u} - \mathbf{u}') W_{k,k'}^s(-\mathbf{u}').
\end{aligned} \tag{A2}$$

where $\Delta\mathbf{n} = \mathbf{n}' - \mathbf{n}$ and $\Delta\mathbf{r}_{\mathbf{n}} = \mathbf{r}_{\mathbf{n}'} - \mathbf{r}_{\mathbf{n}}$. Substituting into (A1) and exploiting the conjugate-symmetry of $W_{k,k'}^s(\mathbf{u})$ gives (7):

$$\begin{aligned}
d'^2 &= (\Delta\bar{\mathbf{D}}^s)^\dagger \left(\mathcal{F}_{\text{DS}} \text{Cov}(\mathbf{d}^s) \mathcal{F}_{\text{DS}}^\dagger \right)^{-1} \Delta\bar{\mathbf{D}}^s \\
&= \Delta_x \Delta_y \int_{\text{Nyq}} \sum_k \sum_{k'} \Delta\bar{D}_k^s(\mathbf{u})^* [(W^s)^{-1}]_{k,k'}^*(\mathbf{u}) \Delta\bar{D}_{k'}^s(\mathbf{u}) d\mathbf{u}.
\end{aligned} \tag{A3}$$

Appendix B: Derivation of the CRLB

In this section we derive the form of the CRLB for $\tilde{\mathbf{A}}(\mathbf{u})$ in the Fourier domain. Using Eq. 25 and the identity $\mathbf{T}^{-1} = \frac{1}{2}\mathbf{T}^\dagger$ we get the CRLB for $\tilde{\mathbf{A}}$ as

$$\begin{aligned}
\text{Cov}(\hat{\tilde{\mathbf{A}}})^{-1} &= (\mathbf{T} \text{Cov}(\boldsymbol{\theta}) \mathbf{T}^\dagger)^{-1} = \frac{1}{4} \mathbf{T} [\text{Cov}(\boldsymbol{\theta})^{-1}] \mathbf{T}^\dagger \tag{B1} \\
&\leq \frac{1}{4} \mathbf{T} \left(\frac{\partial \bar{\mathbf{d}}^s}{\partial \boldsymbol{\theta}} \right)^\top \text{Cov}(\mathbf{d}^s)^{-1} \frac{\partial \bar{\mathbf{d}}^s}{\partial \boldsymbol{\theta}} \mathbf{T}^\dagger = \left(\frac{\partial \bar{\mathbf{d}}^s}{\partial \tilde{\mathbf{A}}}, \frac{\partial \bar{\mathbf{d}}^s}{\partial \tilde{\mathbf{A}}^*} \right)^\dagger \text{Cov}(\mathbf{d}^s)^{-1} \left(\frac{\partial \bar{\mathbf{d}}^s}{\partial \tilde{\mathbf{A}}}, \frac{\partial \bar{\mathbf{d}}^s}{\partial \tilde{\mathbf{A}}^*} \right) = \underline{\mathbf{F}}_{\tilde{\mathbf{A}}},
\end{aligned}$$

where $\underline{\mathbf{F}}_{\tilde{\mathbf{A}}}$ is the Fisher matrix for $\tilde{\mathbf{A}}$. Here the derivatives with respect to \mathbf{A} and \mathbf{A}^* are defined as Wirtinger derivatives, which allows differentiating both real and complex functions with respect to a complex variable (See Ref. 40, ch. A2). This gives $\underline{\mathbf{F}}_{\tilde{\mathbf{A}}} = \begin{pmatrix} \mathbf{F}_{\tilde{\mathbf{A}}} & \tilde{\mathbf{F}}_{\tilde{\mathbf{A}}} \\ \tilde{\mathbf{F}}_{\tilde{\mathbf{A}}}^* & \mathbf{F}_{\tilde{\mathbf{A}}}^* \end{pmatrix}$ with

$$\mathbf{F}_{\tilde{\mathbf{A}}} = \left(\frac{\partial \bar{\mathbf{d}}^s}{\partial \tilde{\mathbf{A}}} \right)^\dagger \text{Cov}(\mathbf{d}^s)^{-1} \left(\frac{\partial \bar{\mathbf{d}}^s}{\partial \tilde{\mathbf{A}}} \right) \text{ and } \tilde{\mathbf{F}}_{\tilde{\mathbf{A}}} = \left(\frac{\partial \bar{\mathbf{d}}^s}{\partial \tilde{\mathbf{A}}} \right)^\dagger \text{Cov}(\mathbf{d}^s)^{-1} \left(\frac{\partial \bar{\mathbf{d}}^s}{\partial \tilde{\mathbf{A}}^*} \right)^*$$

Since Eq. 16 gives $\frac{\partial \bar{Q}(\mathbf{u}', E)}{\partial A_l(\mathbf{u})} = \frac{\partial \bar{q}(E)}{\partial A_l} \delta(\mathbf{u}' - \mathbf{u})$ in the linear approximation, we can calculate

the Jacobian of $\bar{\mathbf{d}}^s$ using the chain rule of differentiation:

$$\begin{aligned} \frac{\partial \bar{d}_{\mathbf{n},k}^s}{\partial \tilde{A}_l(\mathbf{u})} &= \int_0^{E_{\max}} \frac{\partial \bar{d}_{\mathbf{n},k}^s}{\partial \bar{D}_k(\mathbf{u})} \frac{\partial \bar{D}_k(\mathbf{u})}{\partial \bar{Q}(\mathbf{u}, E)} \frac{\partial \bar{Q}(\mathbf{u}, E)}{\partial \tilde{A}_l(\mathbf{u})} dE \\ &= \Delta_x \Delta_y \int_0^{E_{\max}} e^{2\pi i \mathbf{u} \cdot \mathbf{r}_n} H_k(\mathbf{u}, E) \frac{\partial \bar{q}(E)}{\partial A_l} dE = \Delta_x \Delta_y \frac{1}{\bar{q}^{\text{tot}}} \frac{\partial \bar{q}^{\text{tot}}}{\partial A_l} H_{k,l}^{\mathcal{B}}(\mathbf{u}) e^{2\pi i \mathbf{u} \cdot \mathbf{r}_n}. \end{aligned} \quad (\text{B2})$$

Note that the conjugate symmetry of $H_{k,l}^{\mathcal{B}}(\mathbf{u})$ implies that $\frac{\partial \bar{d}_{\mathbf{n},k}^s}{\partial \tilde{A}_l(\mathbf{u})^*} = \left(\frac{\partial \bar{d}_{\mathbf{n},k}^s}{\partial \tilde{A}_l(\mathbf{u})} \right)^* = \Delta_x \Delta_y \frac{1}{\bar{q}^{\text{tot}}} \frac{\partial \bar{q}^{\text{tot}}}{\partial A_l} H_{k,l}^{\mathcal{B}}(-\mathbf{u}) e^{-2\pi i \mathbf{u} \cdot \mathbf{r}_n}$.

Inserted into (25) this gives the elements of $\mathbf{F}_{\tilde{\mathbf{A}}}$ as

$$\begin{aligned} (\mathbf{F}_{\tilde{\mathbf{A}}})_{l,l'}(\mathbf{u}, \mathbf{u}') &= \sum_{\mathbf{n}=-\infty}^{\infty} \sum_{\mathbf{n}'=-\infty}^{\infty} \sum_k \sum_{k'} \left(\frac{\partial \bar{d}_{\mathbf{n},k}^s}{\partial \tilde{A}_l(\mathbf{u})} \right)^* [\text{Cov}(\mathbf{d}^s)^{-1}]_{\mathbf{n},\mathbf{n}',k,k'} \frac{\partial \bar{d}_{\mathbf{n}',k'}^s}{\partial \tilde{A}_{l'}(\mathbf{u}')} \\ &= \frac{\Delta_x^2 \Delta_y^2}{\bar{q}^{\text{tot}2}} \frac{\partial \bar{q}^{\text{tot}}}{\partial A_l} \frac{\partial \bar{q}^{\text{tot}}}{\partial A_{l'}} \sum_k \sum_{k'} H_{k,l}^{\mathcal{B}}(\mathbf{u})^* \sum_{\mathbf{n}=-\infty}^{\infty} \sum_{\mathbf{n}'=-\infty}^{\infty} e^{-2\pi i \mathbf{u} \cdot \mathbf{r}_n} [\text{Cov}(\mathbf{d}^s)^{-1}]_{\mathbf{n},\mathbf{n}',k,k'} e^{2\pi i \mathbf{u}' \cdot \mathbf{r}_{\mathbf{n}'}} H_{k',l'}^{\mathcal{B}}(\mathbf{u}') \\ &= \frac{\Delta_x^2 \Delta_y^2}{\bar{q}^{\text{tot}2}} \frac{\partial \bar{q}^{\text{tot}}}{\partial A_l} \frac{\partial \bar{q}^{\text{tot}}}{\partial A_{l'}} \left[\mathbf{H}^{\mathcal{B}\dagger} \mathcal{F}_{\text{DS}} \text{Cov}(\mathbf{d}^s)^{-1} \mathcal{F}_{\text{DS}}^\dagger \mathbf{H}^{\mathcal{B}} \right]_{l,l'}(\mathbf{u}, \mathbf{u}') \\ &= \frac{1}{\bar{q}^{\text{tot}2}} \frac{\partial \bar{q}^{\text{tot}}}{\partial A_l} \frac{\partial \bar{q}^{\text{tot}}}{\partial A_{l'}} \left[\mathbf{H}^{\mathcal{B}\dagger} \left(\mathcal{F}_{\text{DS}} \text{Cov}(\mathbf{d}^s) \mathcal{F}_{\text{DS}}^\dagger \right)^{-1} \mathbf{H}^{\mathcal{B}} \right]_{l,l'}(\mathbf{u}, \mathbf{u}'), \end{aligned} \quad (\text{B3})$$

where $\mathbf{H}^{\mathcal{B}}$ is the transfer matrix matrix with elements $H_{k,l}^{\mathcal{B}}(\mathbf{u})$. Similarly, the values of $\tilde{\mathbf{F}}_{\tilde{\mathbf{A}}}$ are given by

$$\left(\tilde{\mathbf{F}}_{\tilde{\mathbf{A}}} \right)_{l,l'}(\mathbf{u}, \mathbf{u}') = \frac{1}{\bar{q}^{\text{tot}2}} \frac{\partial \bar{q}^{\text{tot}}}{\partial A_l} \frac{\partial \bar{q}^{\text{tot}}}{\partial A_{l'}} \left[\mathbf{H}^{\mathcal{B}\dagger} \left(\mathcal{F}_{\text{DS}} \text{Cov}(\mathbf{d}^s) \mathcal{F}_{\text{DS}}^\dagger \right)^{-1} \mathbf{H}^{\mathcal{B}} \right]_{l,l'}(\mathbf{u}, -\mathbf{u}'). \quad (\text{B4})$$

Using (A2), we obtain the Fisher matrix elements as

$$\begin{aligned} (\mathbf{F}_{\tilde{\mathbf{A}}})_{l,l'}(\mathbf{u}, \mathbf{u}') &= \frac{1}{\bar{q}^{\text{tot}2}} \frac{\partial \bar{q}^{\text{tot}}}{\partial A_l} \frac{\partial \bar{q}^{\text{tot}}}{\partial A_{l'}} \sum_k \sum_{k'} H_{k,l}^{\mathcal{B}}(\mathbf{u})^* \delta(\mathbf{u} - \mathbf{u}') [W_{d^+}^{-1}]_{k,k'}(-\mathbf{u}) H_{k',l'}^{\mathcal{B}}(\mathbf{u}) \\ &= \frac{1}{\bar{q}^{\text{tot}2}} \frac{\partial \bar{q}^{\text{tot}}}{\partial A_l} \frac{\partial \bar{q}^{\text{tot}}}{\partial A_{l'}} \delta(\mathbf{u} - \mathbf{u}') \text{NEQ}_{l,l'}^{\mathcal{B}}(\mathbf{u}). \end{aligned} \quad (\text{B5})$$

A similar calculation shows that $(\mathbf{F}_{\tilde{\mathbf{A}}})_{l,l'}(\mathbf{u}, \mathbf{u}')$ is proportional to $\delta(\mathbf{u} + \mathbf{u}')$. Since we restrict ourselves to estimating the Fourier coefficient in the right half-plane $\{\mathbf{u} : u > 0 \text{ or } u = 0, v > 0\}$, $(\tilde{\mathbf{F}}_{\tilde{\mathbf{A}}})_{l,l'}(\mathbf{u}, \mathbf{u}') = 0$, which gives (26). The case $\mathbf{u} = \mathbf{0}$ requires special treatment since the fact that $\text{Im } \tilde{\mathbf{A}}(\mathbf{0}) = \mathbf{0}$ makes $\tilde{\mathbf{F}}_{\tilde{\mathbf{A}}}$ singular if $\mathbf{u} = \mathbf{0}$ is included. However, (B5) is sufficient for our purposes since $\text{Cov}(\hat{\tilde{A}}_l(\mathbf{u}))$ can be extrapolated to $\mathbf{u} = \mathbf{0}$ as long as the NEQ does not have a squared delta function at the origin.

REFERENCES

- ^{a)} Author to whom correspondence should be addressed. Electronic mail: matspers@stanford.edu
- ¹K. Taguchi and J. S. Iwanczyk, “Vision 20/20: Single photon counting x-ray detectors in medical imaging,” *Med. Phys.* **40**, 100901 (2013).
- ²P. M. Shikhaliev, T. Xu, and S. Molloy, “Photon counting computed tomography: Concept and initial results,” *Medical Physics* **32**, 427–436 (2005).
- ³H. Bornefalk and M. Danielsson, “Photon-counting spectral computed tomography using silicon strip detectors: a feasibility study,” *Phys. Med. Biol.* **55**, 1999–2022 (2010).
- ⁴P. M. Shikhaliev, “Energy-resolved computed tomography: first experimental results,” *Phys. Med. Biol.* **53**, 5595–5613 (2008).
- ⁵J. Giersch, D. Niederlöhner, and G. Anton, “The influence of energy weighting on x-ray imaging quality,” *Nucl. Instrum. Meth. A* **531**, 68 – 74 (2004), proceedings of the 5th International Workshop on Radiation Imaging Detectors.
- ⁶J. Berglund, H. Johansson, M. Lundqvist, B. Cederström, and E. Fredenberg, “Energy weighting improves dose efficiency in clinical practice: implementation on a spectral photon-counting mammography system,” *Journal of Medical Imaging* **1**, 031003 (2014).
- ⁷J. P. Schlomka, E. Roessl, R. Dorscheid, S. Dill, G. Martens, T. Istel, C. Bumer, C. Herrmann, R. Steadman, G. Zeitler, A. Livne, and R. Proksa, “Experimental feasibility of multi-energy photon-counting K-edge imaging in pre-clinical computed tomography,” *Phys. Med. Biol.* **53**, 4031–4047 (2008).
- ⁸M. Persson, B. Huber, S. Karlsson, X. Liu, H. Chen, C. Xu, M. Yveborg, H. Bornefalk, and M. Danielsson, “Energy-resolved CT imaging with a photon-counting silicon-strip detector,” *Physics in Medicine and Biology* **59**, 6709 (2014).
- ⁹Z. Yu, S. Leng, S. M. Jorgensen, Z. Li, R. Gutjahr, B. Chen, A. F. Halaweish, S. Kappler, L. Yu, E. L. Ritman, and C. H. McCollough, “Evaluation of conventional imaging performance in a research whole-body CT system with a photon-counting detector array,” *Phys. Med. Biol.* **61**, 1572 (2016).
- ¹⁰J. P. Ronaldson, R. Zainon, N. J. A. Scott, S. P. Gieseg, A. P. Butler, P. H. Butler, and N. G. Anderson, “Toward quantifying the composition of soft tissues by spectral CT with Medipix3,” *Med. Phys.* **39**, 6847–6857 (2012).

- ¹¹R. N. Cahn, B. Cederström, M. Danielsson, A. Hall, M. Lundqvist, and D. Nygren, “Detective quantum efficiency dependence on x-ray energy weighting in mammography,” *Medical Physics* **26**, 2680–2683 (1999).
- ¹²T. G. Schmidt, “Optimal “image-based” weighting for energy-resolved CT,” *Med. Phys.* **36**, 3018–3027 (2009).
- ¹³R. E. Alvarez and A. Macovski, “Energy-selective reconstructions in x-ray computerised tomography,” *Phys. Med. Biol.* **21**, 733–744 (1976).
- ¹⁴E. Roessl and R. Proksa, “K-edge imaging in x-ray computed tomography using multi-bin photon counting detectors,” *Phys. Med. Biol.* **52**, 4679 (2007).
- ¹⁵P. Sharp, ed., *ICRU Report 54: Medical Imaging - the Assessment of Image Quality* (International Commission on Radiation Units and Measurements, Bethesda, MD, USA, 1996).
- ¹⁶I. A. Cunningham, “Applied linear-systems theory,” (SPIE Press, Bellingham, Washington, USA, 2000) Chap. 2, pp. 79–159.
- ¹⁷R. J. Acciavatti and A. D. A. Maidment, “A comparative analysis of OTF, NPS, and DQE in energy integrating and photon counting digital x-ray detectors,” *Medical Physics* **37**, 6480–6495 (2010).
- ¹⁸J. Tanguay, S. Yun, H. K. Kim, and I. A. Cunningham, “The detective quantum efficiency of photon-counting x-ray detectors using cascaded-systems analyses,” *Medical Physics* **40**, 041913 (2013), 041913.
- ¹⁹J. Xu, W. Zbijewski, G. Gang, J. W. Stayman, K. Taguchi, M. Lundqvist, E. Fredenberg, J. A. Carrino, and J. H. Siewerdsen, “Cascaded systems analysis of photon counting detectors,” *Medical Physics* **41**, 101907 (2014), 101907.
- ²⁰K. Stierstorfer, “Modeling the frequency-dependent detective quantum efficiency of photon-counting x-ray detectors,” *Medical Physics* , In press.
- ²¹H. Chen, C. Xu, M. Persson, and M. Danielsson, “Optimization of beam quality for photon-counting spectral computed tomography in head imaging: simulation study,” *Journal of Medical Imaging* **2**, 043504 (2015).
- ²²J. Cammin, S. Kappler, T. Weidinger, and K. Taguchi, “Evaluation of models of spectral distortions in photon-counting detectors for computed tomography,” *Journal of Medical Imaging* **3**, 023503 (2016).
- ²³K. Taguchi, M. Zhang, E. C. Frey, X. Wang, J. S. Iwanczyk, E. Nygard, N. E. Hartsough, B. M. W. Tsui, and W. C. Barber, “Modeling the performance of a

- photon counting x-ray detector for CT: Energy response and pulse pileup effects,” *Medical Physics* **38**, 1089–1102 (2011).
- ²⁴J. Tanguay, S. Yun, H. K. Kim, and I. A. Cunningham, “Detective quantum efficiency of photon-counting x-ray detectors,” *Medical Physics* **42**, 491–509 (2015).
- ²⁵S. Faby, J. Maier, S. Sawall, D. Simons, H.-P. Schlemmer, M. Lell, and M. Kachelrieß, “An efficient computational approach to model statistical correlations in photon counting x-ray detectors,” *Medical Physics* **43**, 3945–3960 (2016).
- ²⁶K. Taguchi, C. Polster, O. Lee, K. Stierstorfer, and S. Kappler, “Spatio-energetic cross talk in photon counting detectors: Detector model and correlated poisson data generator,” *Medical Physics* **43**, 6386–6404 (2016).
- ²⁷P. L. Rajbhandary, S. S. Hsieh, and N. J. Pelc, “Effect of spatio-energy correlation in PCD due to charge sharing, scatter, and secondary photons,” *Proc. SPIE* **10132**, 101320V–101320V–8 (2017).
- ²⁸P. M. Shikhaliev, S. G. Fritz, and J. W. Chapman, “Photon counting multi-energy x-ray imaging: Effect of the characteristic x rays on detector performance,” *Medical Physics* **36**, 5107–5119 (2009).
- ²⁹S. Richard and J. H. Siewerdsen, “Cascaded systems analysis of noise reduction algorithms in dual-energy imaging,” *Medical Physics* **35**, 586–601 (2008).
- ³⁰E. Fredenberg, M. Hemmendorff, B. Cederström, M. Åslund, and M. Danielsson, “Contrast-enhanced spectral mammography with a photon-counting detector,” *Medical Physics* **37**, 2017–2029 (2010).
- ³¹M. Yveborg, M. Danielsson, and H. Bornefalk, “Theoretical comparison of a dual energy system and photon counting silicon detector used for material quantification in spectral CT,” *IEEE Transactions on Medical Imaging* **34**, 796–806 (2015).
- ³²H. Chen, M. Danielsson, and C. Xu, “Size-dependent scanning parameters (kVp and mAs) for photon-counting spectral CT system in pediatric imaging: simulation study,” *Physics in Medicine and Biology* **61**, 4105 (2016).
- ³³M. J. Tapiovaara and R. Wagner, “SNR and DQE analysis of broad spectrum x-ray imaging,” *Physics in Medicine and Biology* **30**, 519 (1985).
- ³⁴H. Bornefalk, “Task-based weights for photon counting spectral x-ray imaging,” *Medical Physics* **38**, 6065–6073 (2011).
- ³⁵M. Yveborg, M. Persson, and H. Bornefalk, “Optimal

- frequency-based weighting for spectral x-ray projection imaging,” *IEEE Transactions on Medical Imaging* **34**, 779–787 (2015).
- ³⁶H. H. Barrett and K. J. Myers, *Foundations of Image Science* (John Wiley & Sons, Inc., Hoboken, New Jersey, 2004).
- ³⁷E. Roessl and C. Herrmann, “Cramér-Rao lower bound of basis image noise in multiple-energy x-ray imaging,” *Physics in Medicine & Biology* **54**, 1307 (2009).
- ³⁸E. Roessl, B. Brendel, K. J. Engel, J. P. Schlomka, A. Thran, and R. Proksa, “Sensitivity of photon-counting based k-edge imaging in x-ray computed tomography,” *IEEE Transactions on Medical Imaging* **30**, 1678–1690 (2011).
- ³⁹S. M. Kay, *Fundamentals of Statistical Signal Processing: Estimation Theory* (Prentice Hall PTR, Upper Saddle River, New Jersey, 1993).
- ⁴⁰P. J. Schreier and L. L. Scharf, *Statistical Signal Processing of Complex-Valued Data: The Theory of Imp* (Cambridge University Press, 2010).
- ⁴¹R. E. Alvarez, “Near optimal energy selective x-ray imaging system performance with simple detectors,” *Medical Physics* **37**, 822–841 (2010).
- ⁴²R. Alvarez and E. Seppi, “A comparison of noise and dose in conventional and energy selective computed tomography,” *IEEE Transactions on Nuclear Science* **26**, 2853–2856 (1979).
- ⁴³L. A. Lehmann, R. E. Alvarez, A. Macovski, W. R. Brody, N. J. Pelc, S. J. Riederer, and A. L. Hall, “Generalized image combinations in dual KVP digital radiography,” *Medical Physics* **8**, 659–667 (1981).
- ⁴⁴F. S. Philippe T. Pinard, Hendrix Demers and R. Gauvin, “pyPENELOPE software package,” pypenelope.sourceforge.net/.
- ⁴⁵J. S. Francesc Salvat, Jos M. Fernndez-Varea, “PENELOPE-2006: a code system for monte carlo simulation of electron and photon transport,” <https://www.oecd-neo.org/science/pubs/2006/nea6222-penelope.pdf>.
- ⁴⁶A. M. Hernandez and J. M. Boone, “Tungsten anode spectral model using interpolating cubic splines: Unfiltered x-ray spectra from 20 kV to 640 kV,” *Medical Physics* **41**, 042101 (2014).
- ⁴⁷J. Punnoose, J. Xu, A. Sisniega, W. Zbijewski, and J. H. Siewerdsen, “Technical note: spektr 3.0-A computational tool for x-ray spectrum modeling and analysis,” *Medical Physics* **43**, 4711–4717 (2016).

⁴⁸M. J. Berger, J. H. Hubbell, S. M. Seltzer, J. Chang, J. S. Coursey, R. Sukumar, D. S. Zucker, and K. Olsen, “XCOM: Photon Cross Section Database,” <http://physics.nist.gov/xcom>. National Institute of Standards and Technology, Gaithersburg, MD (2005).